Applied Catalysis B: Environment and Energy 390 (2026) 126552

Contents lists available at ScienceDirect

Applied Catalysis B: Environment and Energy

journal homepage: www.elsevier.com/locate/apcatb

Metal-organic framework-derived carbons coupled CdSe quantum dots for solar H_2 production beyond visible region

Chien-Yi Wang [a], Yu-Chen Wei [a], Yu-Chang Lin [b], Sudhakar Narra [c], Chun-Yi Chen [d], Tso-Fu Mark Chang [d], Masato Sone [d], Ying-Chih Pu [e], Eric Wei-Guang Diau [c,*], Yan-Gu Lin [a,b,**], Cheng-Yu Wang [a,*], Yung-Jung Hsu [a,d,f,**]

[a] Department of Materials Science and Engineering, National Yang Ming Chiao Tung University, Hsinchu 300093, Taiwan
[b] National Synchrotron Radiation Research Center, Hsinchu 30076, Taiwan
[c] Department of Applied Chemistry and Institute of Molecular Science, National Yang Ming Chiao Tung University, Hsinchu 300093, Taiwan
[d] Institute of Integrated Research, Institute of Science Tokyo, Kanagawa 226-8503, Japan
[e] Department of Materials Science, National University of Tainan, Tainan 70005, Taiwan
[f] Center for Emergent Functional Matter Science, National Yang Ming Chiao Tung University, Hsinchu 300093, Taiwan

ARTICLE INFO

Keywords:
MOF-derived carbons
CdSe
Solar H_2 production
Near infrared

ABSTRACT

This study introduces a versatile photocatalyst paradigm for achieving photocatalytic H_2 production extending beyond the visible region by coupling metal-organic framework (MOF)-derived carbons with CdSe quantum dots. Zeolitic imidazolate framework-67 (ZIF-67) serves as the parent MOF, enabling the synthesis of ZIF-derived amorphous carbons (ZDAC) and crystalline carbons (ZDCC). These materials are subsequently coupled with CdSe quantum dots to form ZDAC/CdSe and ZDCC/CdSe composites, respectively. ZDCC/CdSe outperforms ZDAC/CdSe in H_2 production under AM 1.5 G illumination, achieving notable quantum yields of up to 6.4 % at 420 nm and 3.9 % at 800 nm without the addition of co-catalysts. This superior performance highlights the ability of ZDCC/CdSe to effectively harness both visible and near infrared (NIR) light, addressing a long-standing challenge in utilizing the untapped NIR energy from the solar spectrum. Furthermore, long-term stability tests demonstrate the robustness of ZDCC/CdSe over extended operational periods, overcoming the critical issue of photocorrosion typically associated with CdSe-based photocatalysts. By providing an efficient, durable, and broad-spectrum responsive platform for solar H_2 production, this study lays a solid foundation for addressing energy sustainability challenges. It advances the field of solar fuel generation by emphasizing the importance of harvesting energy from the entire solar spectrum, paving the way for innovative solutions to global energy demands.

1. Introduction

The 21st century is defined by growing concerns over fossil fuel depletion and global warming, underscoring the urgent need for sustainable and renewable energy solutions. Among these, solar H_2 production using semiconductor photocatalysts emerges as a particularly promising technology [1,2]. This technology utilizes solar energy to efficiently split water, producing H_2 in a simple and environmentally friendly manner [3,4]. However, the process remains hindered by low efficiency, necessitating the development of advanced materials to enhance light absorption and improve charge separation [5–7]. In this context, CdSe quantum dots have emerged as promising photocatalysts for H_2 production due to their optimally positioned band gap, which supports effective photon harvesting and favorable photocatalytic reaction kinetics [8,9]. Despite these advantages, the practical application of CdSe is significantly limited by its poor stability, particularly its susceptibility to photocorrosion, which hampers long-term durability and utility [9–11]. Accordingly, integrating CdSe with complementary components to mitigate photocorrosion is essential for its broad deployment in photocatalytic applications.

* Corresponding authors.
** Corresponding authors at: Department of Materials Science and Engineering, National Yang Ming Chiao Tung University, Hsinchu 300093, Taiwan.
E-mail addresses: diau@nycu.edu.tw (E.W.-G. Diau), lin.yg@nsrrc.org.tw (Y.-G. Lin), ChengYuWang@nycu.edu.tw (C.-Y. Wang), yhsu@cc.nctu.edu.tw, yhsu@nycu.edu.tw (Y.-J. Hsu).

https://doi.org/10.1016/j.apcatb.2026.126552
Received 11 January 2026; Received in revised form 6 February 2026; Accepted 8 February 2026
Available online 9 February 2026
0926-3373/© 2026 Elsevier B.V. All rights are reserved, including those for text and data mining, AI training, and similar technologies.

Metal-organic frameworks (MOFs), consisting of central metals intricately coordinated with organic ligands, have garnered significant attention over the past decade for their exceptional properties and diverse applications [12,13], including photocatalysis. Their ultrahigh specific surface area and remarkable porosity provide abundant active sites for catalytic reactions, while their adjustable chemical compositions enable property tailoring to specific needs [14,15]. Furthermore, the structural tunability of MOFs allows precise control over pore size, shape, and surface functionality [16–19]. Despite these advantages, several challenges hinder their practical use in photocatalysis. MOFs are often vulnerable to structural degradation in aqueous environments [20] or upon light exposure [21], compromising their integrity. Additionally, poor electrical conductivity limits efficient charge transfer, diminishing their catalytic performance [22–24]. The relatively large band gap of MOFs further narrows their light absorption range, reducing solar energy utilization and overall photocatalytic efficiency [25–27]. To address these limitations, MOFs have been increasingly used as templates to synthesize MOF-derived materials, such as metals [28], metal oxides [29], single atoms [30], high-entropy alloys [31], and sulfides [32]. These derived materials exhibit enhanced stability, improved conductivity, and retained porous characteristics, making them better suited for demanding conditions [33–35]. The tunable microstructures of MOF-derived materials further enable precise optimization of photocatalytic properties, significantly advancing their application potential.

Carbon-based materials have been extensively explored as photocatalysts owing to their high chemical stability, large specific surface area, and favorable electronic conductivity, which are beneficial for light-induced charge transport and surface redox reactions. In particular, carbon materials can effectively suppress charge recombination and facilitate interfacial electron transfer, making them attractive platforms for photocatalytic energy conversion and environmental remediation [36,37]. However, conventional carbon materials often suffer from limited control over porosity, active site distribution, and structural uniformity, which restricts their photocatalytic performance. MOF-derived carbon materials have recently emerged as a promising class of carbon-based photocatalysts, as they inherit the well-defined porous architecture and tunable composition of their parent MOFs while exhibiting the superior stability and conductivity of carbon frameworks. The controlled carbonization of MOFs enables the rational modulation of pore structure, surface chemistry, and heteroatom doping, thereby enhancing light absorption, charge separation, and catalytic activity [38]. As a result, MOF-derived carbons have demonstrated remarkable performance in a variety of photocatalytic applications, including solar H_2 production, CO_2 reduction, and pollutant degradation [39–41]. These advantages highlight the potential of MOF-derived carbon materials as efficient and robust photocatalytic platforms for energy conversion.

In this study, zeolitic imidazolate framework-67 (ZIF-67) was utilized as the precursor material and annealed under different atmospheres to synthesize ZIF-derived amorphous carbons (ZDAC) and crystalline carbons (ZDCC). These materials were subsequently coupled with CdSe quantum dots to fabricate ZDAC/CdSe and ZDCC/CdSe composites designed for solar H_2 production. For comparison purposes, zeolitic imidazolate framework-8 (ZIF-8) was also synthesized, annealed, and coupled with CdSe. Charge transfer dynamics at the interface and surface of the composites were thoroughly investigated using time-resolved photoluminescence (PL), μs- and fs-transient absorption (TA) spectroscopy. Additionally, site-selective photodeposition experiments were conducted to validate the proposed charge transfer mechanism. This work demonstrates a robust strategy for integrating MOF-derived carbons with semiconductor quantum dots, offering a practical pathway for solar H_2 production.

2. Experimental section

2.1. Synthesis of CdSe

CdSe quantum dots were synthesized based on a previous report [11]. Typically, 2.0 mL of 0.15 M $Cd(NO_3)_2$ was mixed with 2.6 mL of 1.0 M *L*-cysteine in a vial, and the pH was adjusted to 10.0 using 1.0 M NaOH. The mixed solution was then diluted to 100 mL with deionized (DI) water, followed by adding 0.375 mL of 0.2 M Na_2SeSO_3 solution. The reaction solution was stirred at room temperature for 1 h. Finally, the obtained yellow solution was centrifuged and washed with isopropanol (IPA) twice.

2.2. Synthesis of ZIF-67

In a typical procedure, 1.0 mmol of $Co(NO_3)_2{\cdot}6\,H_2O$ was dissolved in 3.0 mL DI water and then dropped into 20 mL of DI water, which contained 4 mmol of 2-methylimidazole. The solution was stirred for 24 h. The obtained precipitates were centrifuged and washed twice with IPA and dried under a vacuum.

2.3. Synthesis of ZIF-8

In a typical procedure, 1.0 mmol of $Zn(NO_3)_2{\cdot}6\,H_2O$ was dissolved in 3.0 mL of DI water and then added dropwise into 20 mL of DI water containing 4 mmol of 2-methylimidazole. The solution was stirred for 24 h. The resulting precipitates were collected by centrifugation, washed twice with IPA, and dried under vacuum.

2.4. Synthesis of ZIF-derived carbons

The as-obtained ZIF-67 powder was annealed at 600 °C for 3 h at a heating rate of 10°C /min under an Ar atmosphere, and cooled to room temperature to obtain the black powder. The resultant ZIF-derived amorphous carbons were denoted as ZDAC. In a separate synthetic procedure, the as-obtained ZIF-67 powder was annealed at 400 °C for 30 min at a heating rate of 10 °C/min under a pure H_2 atmosphere, and cooled to room temperature to obtain the gray powder. The resultant ZIF-derived crystalline carbons were denoted as ZDCC. On the other hand, the as-obtained ZIF-8 powder was annealed at 400 °C for 30 min at a heating rate of 10 °C/min under a pure H_2 atmosphere, and cooled to room temperature to obtain the powder. The resultant ZIF-8-derived carbon was denoted as ZnDC.

2.5. Coupling ZDAC, ZDCC, and ZnDC with CdSe

In a typical procedure, 2.0 mL of 0.15 M $Cd(NO_3)_2$ was mixed with 2.6 mL of 1.0 M *L*-cysteine in a vial (capacity = 150 mL), and the pH was adjusted to 10.0 using 1.0 M NaOH. The resulting solution (Cd^{2+} precursor solution) was diluted to 80 mL with DI water. The as-synthesized ZDAC, ZDCC, and ZnDC powders were separately dissolved in 20 mL of DI water, followed by the addition of the above solution under continuous stirring. Afterward, 0.375 mL of 0.2 M Na_2SeSO_3 solution (Se^{2-} precursor solution) was introduced, and the reaction mixture was stirred at room temperature for 1 h. Finally, the obtained solution was subject to centrifugation at 8800 rpm and washed twice with IPA. The resultant ZDAC-coupled CdSe, ZDCC-coupled CdSe, and ZnDC-coupled CdSe were respectively denoted as ZDAC/CdSe, ZDCC/CdSe, and ZnDC/CdSe. Note that the amounts of ZDAC, ZDCC, and ZnDC were adjusted to enable the synthesis of ZDAC/CdSe, ZDCC/CdSe, and ZnDC/CdSe with controlled CdSe loadings.

2.6. Characterizations

The morphology and microstructure were analyzed by a field-emission scanning electron microscope (SEM) (Hitachi, SU-8010) and

a high-resolution transmission electron microscope (HRTEM) (JEOL, JEM-F200) equipped with selected-area electron diffraction (SAED) and an energy dispersive X-ray spectrometer (EDS). The crystalline structure was measured by X-ray powder diffraction (XRD) (Bruker, D2 Phaser). The chemical compositions of the samples were examined with X-ray photoelectron spectroscopy (XPS, Thermo Fisher Scientific, ESCALAB Xi+) using a monochromatic Al Kα X-ray source. The XPS fitting was performed using a consistent, literature-standard protocol chosen for reliability and physical interpretability, as detailed in the Experimental section of revised manuscript. Briefly, all binding energies were calibrated to the C 1 s peak at 284.8 eV. A Shirley background was applied to all spectra, and peaks were deconvoluted with mixed Lorentzian–Gaussian line shapes. Full widths at half maximum were constrained to be comparable for peaks assigned to the same chemical state. For spin-orbit-split core levels, the energy separations and area ratios were fixed to accepted values from the literature. Fit quality was quantified using χ^2, and the resulting values were 1.0577 for Co 2p, 1.1688 for C 1 s, 1.0133 for Cd 3d, and 1.0533 for Se 3d, which are close to unity, indicating satisfactory fits and reliable peak assignments. The optical properties were studied with a UV–visible-near infrared (NIR) absorption spectrophotometer (Hitachi, U-3900H) attached with an integrating sphere, and a PL spectrometer (Hitachi, F-4500). The Brunauer-Emmett-Teller (BET) specific surface areas were measured with N_2 adsorption-desorption isotherms (Micromeritics ASAP 2060). Electrochemical impedance spectroscopy (EIS) spectra were conducted at an open circuit potential in a range of 10^5–10^{-2} Hz under AM 1.5 G irradiation (100 mW cm^{-2}) produced by a solar simulator (Newport, LCS-100, 94011 A). The band structure of the samples was determined by ultraviolet photoelectron spectroscopy (UPS) spectra (Thermo Fisher Scientific, ESCALAB Xi^+) using He I ($h\upsilon$ = 21.22 eV) as the energy source. The elemental compositions of ZDAC and ZDCC were quantitatively analyzed using inductively coupled plasma mass spectrometry (ICP-MS, Thermo Fisher Scientific, iCAP TQ). Raman spectra were collected on a Thermo Fisher Scientific DXR2 spectroscope using an Ar source laser (λ = 532 nm). Time-resolved PL data were collected using a customized designed single photon counting system comprising a sub-second pulsed diode laser (λ = 320 nm, PicoQuant, PLD320) with an instrument response function (IRF) that enables temporal resolution down to 50 ps. The data were fitted with the following bi-exponential equation to obtain the quantitative information.

$$I(t) = \sum_{n=1}^{2} A_n \exp(-\frac{t}{\tau_n})$$

where τ and A represented the decay lifetime and the corresponding amplitude of PL signals. By averaging the two lifetime components, an intensity-average lifetime was calculated using the following equation [42]:

$$<\tau>=\frac{A_1\tau_1^2 + A_2\tau_2^2}{A_1\tau_1 + A_2\tau_2}$$

2.7. Photocatalytic H_2 production

An AM 1.5 G irradiation (100 mW cm^{-2}) generated by a solar simulator (Newport, LCS-100, 94011 A) was used to conduct the photocatalytic H_2 production experiments. 10 mg of sample powder was dispersed in 10.0 mL of 0.5 M *L*-ascorbic acid aqueous electrolyte in a customized reactor (20 mL capacity). Before illumination, the solution was purged with Ar for 1 h to remove the gas species that may disturb the experiment. During the photocatalytic process, the gas products were automatically introduced to a gas chromatography (GC) system (Agilent, 990 Micro GC). The apparent quantum yield (AQY) of H_2 production was determined by conducted H_2 production experiments under monochromatic illumination produced by a 150 W xenon lamp coupled with a monochromator (Horiba, Tunable PowerArc, 0.2 m, 1200 gr mm^{-1}, dispersion = 5 nm). The number of incident photons was measured with an optical power meter (Newport, 843-R). The value of AQY was calculated by the following equation.

$$\text{AQY}\ (\%) = \frac{\text{number of reacted electrons}}{\text{number of incident photons}} \times 100\ \%$$

$$= \frac{2 \times \text{evolved hydrogen molecules}}{\text{number of incident photons}} \times 100\ \%$$

2.8. μs-TA spectroscopy

The μs-TA spectrometer consists of an Nd/YAG laser (LOTIS LS-2134, 8 ns pulse width) coupled with a wavelength-tunable system (LOTIS LT-2211) at 390 nm. The frequency of the laser flash was 10 Hz, and the intensity of the laser pulse was 200 μJ/cm^2. The probe light source is a 150 W Xe lamp (GLORIA-X150A) equipped with band-pass filters (Andover Corporation). A silicon photodiode (Zolix DSi 200) was used to detect transmitted photons. The collected data were processed using a digital delay/pulse generator (Stanford Research Systems, DG535) and recorded with an oscilloscope (GDS-2302A) on the timescale of μs. The sample powders (1 mg) were dispersed in pure DI water (3 mL), in DI water (3 mL) containing an electron scavenger (0.1 mM benzoquinone), or in 0.5 M *L*-ascorbic acid aqueous electrolyte (3 mL) for μs-TA measurements.

2.9. fs-TA spectroscopy

The fs-TA measurements were performed using an Excipro fs transient absorption spectrometer. The spectroscopic system utilizes an ultrashort pulse amplifier (Legend USP, 2.2 mJ, 35 fs, 795 nm, and 1kHZ). The output of the amplifier is split into two parts. One part is used to pump an optical parametric amplifier (OPA) to generate 325 nm by utilizing the fourth harmonic generation module of the OPA. The other part is attenuated further, and a weak portion of the fundamental is utilized to pump a 3 mm CaF_2 substrate mounted on a rotation stage. The white light continuum generated is collected using a curved mirror and filtered using a short pass filter to limit the spectral width of the continuum to 350–750 nm. The time-resolved spectra are measured by optically delaying the pump pulses with respect to the probe pulses. The group velocity dispersion of the white light is corrected by measuring optical kerr signals of the solvent (water) under identical conditions to the pump-probe experiments. For fs pump-probe experiments, the sample powders (2 mg) were dispersed in DI water (1 mL), sonicated, and transferred into a quartz cell (2 mm optical path). The pump pulse energy was set to 230 nJ. The kinetics data of ground-state bleach were fitted by convoluting multi-exponential functions with the apparatus response function to fit the whole decay profile.

2.10. X-ray absorption

X-ray absorption spectroscopic (XAS) measurements were performed at beamline 44 A of the Taiwan Photon Source and beamline 13B of the Taiwan Light Source, utilizing the total fluorescence yield mode. The in-situ XAS experiments were carried out under additional irradiation to simulate the illumination conditions of photocatalytic reactions. The light source used for additional irradiation was a triple-A solar simulator equipped with an AM 1.5 G filter (HAL-320, Asahi Spectra). Soft-XAS experiments were performed at beamline 20 A of the Taiwan Light Source, utilizing a 6-m high-energy spherical-grating monochromator to probe the electronic structure by X-ray absorption near-edge structure (XANES) spectroscopy. Measurements were conducted in an ultrahigh-vacuum chamber (UHV, 10^{-9} torr), with data collected using the total fluorescence yield method, offering a resolving power of E/ΔE of 8×10^3. The in-situ soft-XAS experiments were carried out under additional irradiation in the presence of 0.5 M *L*-ascorbic acid to simulate the operation conditions of photocatalytic reactions.

2.11. Site-selective photodeposition

For the photodeposition of Pt, 5.0 mg of ZDCC/CdSe was dispersed in 40 mL of 0.5 mM $H_2PtCl_6{\cdot}6\ H_2O$ containing 10 vol% methanol [43,44]. The solution was illuminated under AM 1.5 G irradiation (100 mW cm^{-2}) for 1 h. Afterwards, the solution was centrifuged and washed with methanol twice. For the photodeposition of PbO_2 [43,44], the experimental procedures were identical to those of photodeposition of Pt except that 0.5 mM $Pb(NO_3)_2$ was used as the metal precursor.

3. Results and discussion

3.1. Microstructure and chemical states

The synthesis of ZIF-67-derived carbon/CdSe composites was achieved via a ship-in-a-bottle method, as illustrated schematically in Scheme 1. ZIF-67 powders were annealed under Ar and H_2 atmospheres to produce ZDAC and ZDCC, respectively. Annealing in an Ar atmosphere resulted in relatively large Co particles due to prolonged reaction times, allowing particle growth and aggregation. Conversely, the higher reducing capacity of H_2 significantly shortened the reaction time, yielding much smaller Co particles. The size difference of Co particles directly influenced the derived carbon structure. In the H_2 atmosphere, the highly reactive, tiny Co particles catalyzed the formation of carbon nanodiamonds (CND) as primary structures. As annealing proceeded, sp^3-carbon detachment from the surface resulted in dangling bonds [45,46], leading to graphitization and the formation of sp^2-carbon shells, which partially transformed into carbon onion shells (COS). This process explained the crystalline carbon structure of ZDCC. By contrast, the less reactive and larger Co particles in the Ar atmosphere caused incomplete pyrolysis of the organic ligands, resulting in amorphous carbons in ZDAC. Upon exposure to air, the diminutive Co particles in ZDCC oxidized completely to Co_3O_4, while the larger Co particles in ZDAC underwent partial oxidation. In summary, ZDAC comprised large Co/Co_3O_4 particles embedded in amorphous carbons, whereas ZDCC contained tiny Co_3O_4 particles enclosed within crystalline carbons featuring CND and COS. The ZDAC and ZDCC were subsequently coupled with CdSe quantum dots via a cysteine-assisted aqueous synthetic approach, producing composites denoted as ZDAC/CdSe-X and ZDCC/CdSe-X, where X represents the weight percentage of CdSe.

The ZIF-derived carbons, ZDAC and ZDCC, were initially characterized using SEM and TEM. Both materials exhibited a flower-like morphology with rough surfaces, as shown in Fig. S1 (supplementary material). TEM analysis provided further insights into their crystallographic structures. For ZDAC, the TEM image of Fig. 1(a) confirmed the presence of Co/Co_3O_4 particles within amorphous carbon, with an average particle size of approximately 6.8 nm. HRTEM revealed lattice fringes with an inter-layer spacing of 0.19 nm, corresponding to the (111) plane of face-centered cubic (fcc) Co. In contrast, TEM analysis of ZDCC in Fig. 1(b) indicated the formation of CND with well-defined lattice fringes, signifying high crystallinity. COS was also observed on

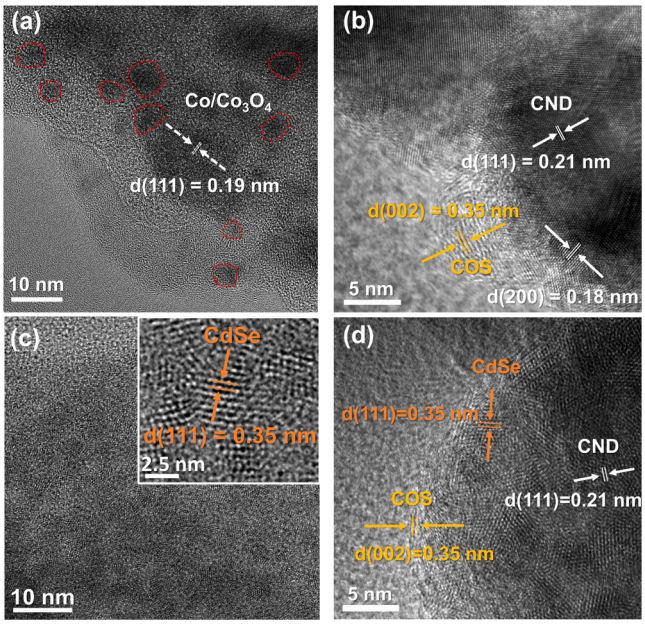

Fig. 1. TEM images of (a) pure ZDAC, (b) pure ZDCC, (c) pure CdSe, (d) ZDCC/CdSe-20 %.

the outer layer of the CND. The inter-planar spacings of 0.18 and 0.21 nm corresponded to the (200) and (111) planes of hexagonal close-packed (hcp) carbon, while the inter-layer spacing of COS was measured as 0.35 nm, attributable to the (002) plane of hcp carbon. Due to their small size, the Co_3O_4 particles in ZDCC were challenging to detect directly. Fig. 1(c-d) presents TEM images of pure CdSe and ZDCC/CdSe composites. The embedded CdSe in ZDCC/CdSe was clearly observed, with an inter-layer spacing of 0.35 nm corresponding to the (111) plane of zinc blende CdSe. Elemental analysis by TEM-EDS in Fig. S2 (supplementary material) showed uniform distribution of Cd, Se, and Co across the composite structure. Importantly, the spatial distribution of Cd and Se signals is consistent with the corresponding microstructural features, confirming the formation of CdSe in the ZIF-derived carbons. The existence of CdSe is further corroborated by validating the assignment of CdSe lattice spacings. As shown in Fig. S3 (supplementary material), two distinct lattice fringes with interplanar spacings of 0.35 nm and 0.21 nm and a directional angle of 35 ° can be measured on ZDCC/CdSe-20 %. According to the theoretical values of interplanar distance, these two spacings are respectively assigned to (111) and (220) planes of cubic CdSe. For a cubic lattice, the angle between two crystal planes ($h_1\ k_1\ l_1$) and ($h_2\ k_2\ l_2$) can be calculated using Equation S1 (supplementary material). For a cubic CdSe crystal, the directional angle between (111) and (220) planes is computed to be 35.26 °, which is in good agreement with the experimentally observed angle of 35 °. XRD analysis further elucidated the crystallographic properties of the

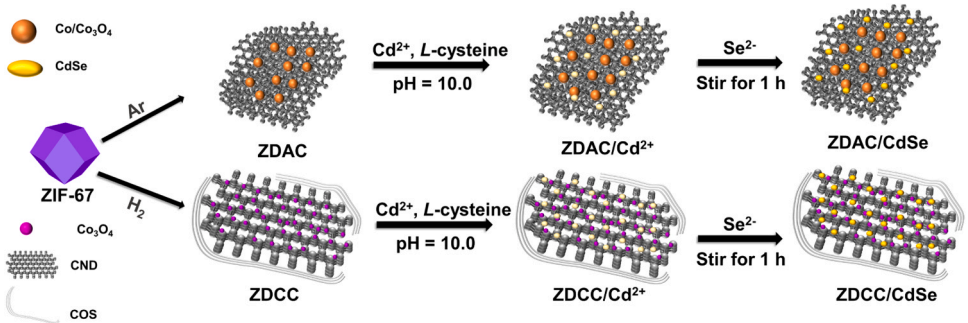

Scheme 1. Illustration of the synthetic procedures for ZDAC/CdSe and ZDCC/CdSe.

samples. In Fig. S4 (supplementary material), the diffraction peaks corresponding to Co metal (JCPDS No. 15–0806) were observed in ZDAC and ZDAC/CdSe, whereas Co_3O_4 signals were absent in ZDCC and ZDCC/CdSe, likely due to the poor crystallinity of the minute Co_3O_4 particles. CdSe quantum dots exhibited broad diffraction peaks due to quantum size effects. For both ZDAC/CdSe and ZDCC/CdSe, the peaks corresponding to zinc blende CdSe (JCPDS No. 19–0191) became more pronounced with increasing CdSe concentration. Notably, no impurity-related peaks were observed, confirming the high chemical and structural integrity of the composites. To validate the phase identification results, SAED patterns of the four samples were further investigated in Fig. S4 (supplementary material). The recorded ring patterns correspond well with the crystallographic structure of the respective components. The particle size distribution for pure CdSe and Co/Co_3O_4 particles of pure ZDAC was also analyzed from the corresponding low-magnification TEM images. As shown in Fig. S6 and S7 (supplementary material), pure CdSe possessed a size of 1.83 ± 0.23 nm, while Co/Co_3O_4 of pure ZDAC had a size of 6.59 ± 1.00 nm. For Co_3O_4 particles of pure ZDCC, it was, however, improbable to determine their size distribution from TEM images because of the small size of Co_3O_4. On the other hand, to quantify Co loading, ICP-MS analysis was performed on pure ZDAC and pure ZDCC. Based on four replicate measurements, the average Co contents were 24.91 wt% for pure ZDAC and 74.46 wt% for pure ZDCC. The substantially higher Co content in ZDCC is plausibly attributable to the H_2 atmosphere used during annealing, which creates a more reducing environment that promotes more complete decomposition of organic ligands and a greater loss of the carbonaceous matrix, thereby enriching the residual Co fraction. These values are consistent with literature trends for ZIF-derived carbons, whose Co contents vary widely with pyrolysis temperature and atmosphere (typically from 10 to 70 wt%) [47–51]. The Co value of ZDCC lies at the upper end of this range, as expected under strongly reducing conditions.

XPS was employed to analyze the chemical states of the elements in the samples. As shown in Fig. S8(a-b) (supplementary material), the Co 2p spectra for both ZDAC and ZDCC were deconvoluted into Co^{2+} and Co^{3+} peaks with doublets of Co $2p_{3/2}$ and Co $2p_{1/2}$. The presence of satellite peaks confirmed the composition of Co_3O_4 in both samples. In ZDAC, the co-existence of metallic Co alongside Co^{2+}/Co^{3+} indicated partial oxidation of Co. In contrast, the absence of metallic Co signals in ZDCC confirmed its exclusive composition of oxidized Co. The chemical states of carbon were analyzed in Fig. S8(c-d) (supplementary material). For ZDAC, the dominant sp^2-carbon signal, characteristic of graphitic structures [52], indicated amorphous carbon. Conversely, ZDCC exhibited a predominant sp^3-carbon signal, consistent with CND as primary structures. Additionally, a π-π* satellite peak was observed for ZDCC, signifying the presence of active π-electrons induced by COS [53,

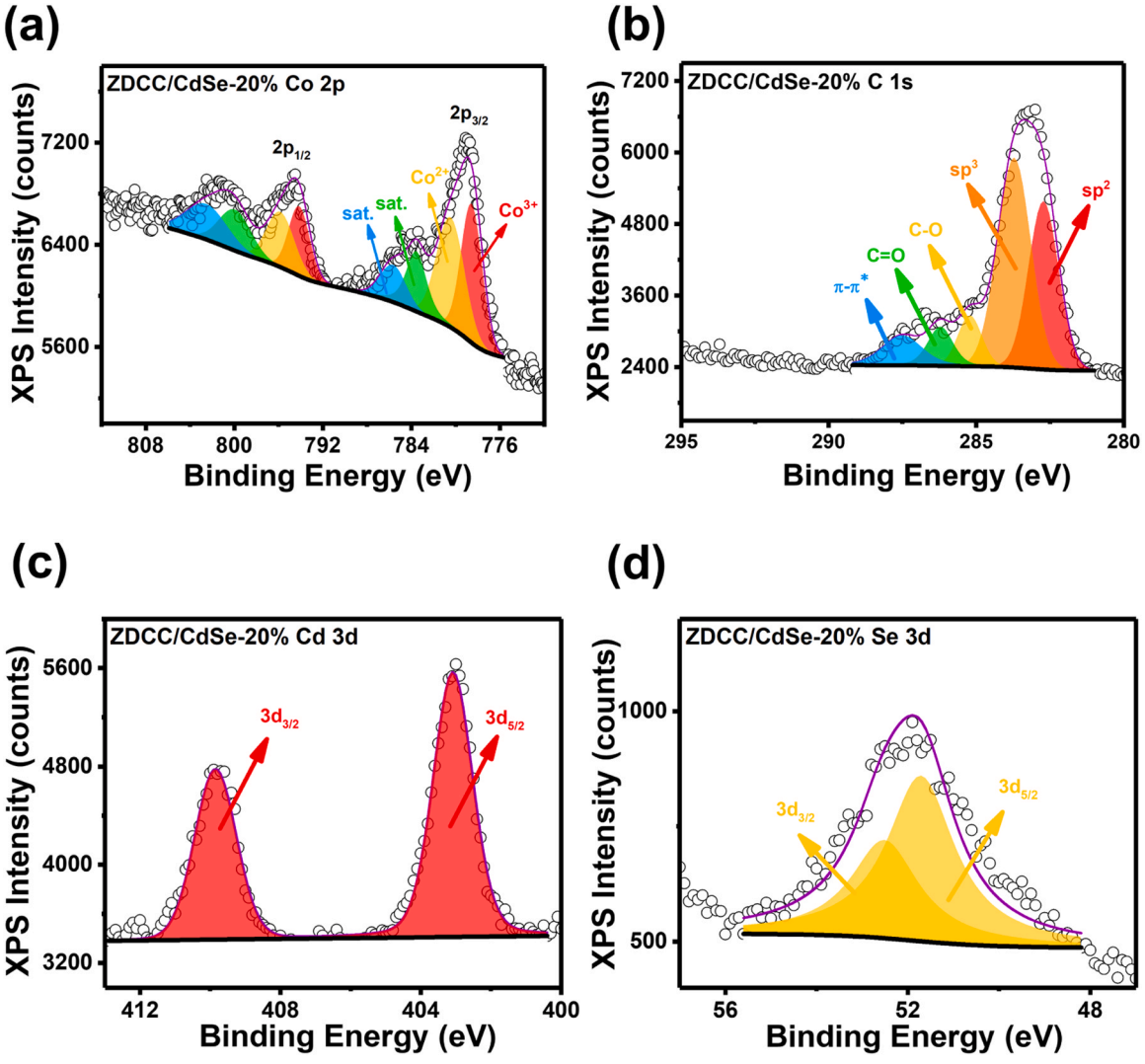

Fig. 2. XPS spectra of (a) Co 2p, (b) C 1 s, (c) Cd 3d, (d) Se 3d for ZDCC/CdSe-20 %. Note that black open circles denote raw data and the purple solid line corresponds to the cumulative fit.

54]. These π-π interactions enhance electron delocalization, contributing to improved electrical conductivity [55]. When ZDCC was coupled with CdSe, the chemical states of Co, C, Cd, and Se remained intact. As shown in Fig. 2(a-b), the Co 2p and C 1 s spectra of ZDCC/CdSe retained the spectral characteristics of pure ZDCC. Additionally, Fig. 2(c-d) revealed Cd 3d and Se 3d peaks exclusive to CdSe, indicating the preservation of chemical integrity in ZDCC/CdSe composites. This consistency highlights the structural and compositional stability of the composite materials.

The chemical states and structural arrangement of oxidized Co in pure ZDCC and ZDCC/CdSe were further investigated using XANES spectroscopy. As shown in Fig. S9(a) (supplementary material), all Co-related samples displayed a pre-edge peak at approximately 7710 eV, corresponding to the 1 s to 3d electron transition indicative of the electronic structure and local symmetry around Co centers. Notably, the XANES spectra of CoO and Co_3O_4 exhibited pronounced white line features near 7730 eV, a characteristic marker of oxidized Co (Co^{2+}/Co^{3+}) [56]. Both pure ZDCC and ZDCC/CdSe-20 % demonstrated white line features consistent with Co_3O_4, confirming the exclusive composition of Co_3O_4 in these samples. To further examine the local structural arrangement around Co, extended X-ray absorption fine structure (EXAFS) analysis was conducted. As shown in Fig. S9(b) (supplementary material), the EXAFS spectra of pure ZDCC and ZDCC/CdSe-20 % revealed a distinct first-shell peak at approximately 1.44 Å, corresponding to Co-O scattering paths characteristic of Co_3O_4 coordination [57]. Additionally, Co-Co interaction peaks for both samples exhibited shifts relative to the Co foil, aligning instead with the octahedral and tetrahedral Co-Co bonds typical of Co_3O_4 [58]. The findings from EXAFS analysis corroborated the XANES results, conclusively confirming that the Co species in pure ZDCC and ZDCC/CdSe are exclusively composed of Co_3O_4.

3.2. Optical properties and charge dynamics

The UV–visible absorption spectra of ZDAC/CdSe and ZDCC/CdSe exhibited significant absorption across the UV to visible regions. As shown in Fig. 3(a-b), the absorption edge corresponding to CdSe became increasingly prominent in ZDAC/CdSe and ZDCC/CdSe as the CdSe loading concentration increased. This observation confirmed the successful incorporation of CdSe into ZDAC and ZDCC, highlighting the tunable optical properties of the composites in response to CdSe concentration. The steady-state PL spectra of the composites, presented in Fig. 3(c-d), were analyzed to investigate possible charge transfer scenarios. The PL signal of pure CdSe, characterized by a broad emission band centered at 560 nm, served as a reference. A significant quenching of PL intensity was observed when CdSe was coupled with ZDAC or ZDCC. This pronounced reduction in PL emission indicated that both ZDAC and ZDCC affected charge carrier transfer for CdSe, suppressing charge recombination to depress the PL emission. The diminished PL intensity in ZDAC/CdSe and ZDCC/CdSe demonstrated the prevalence

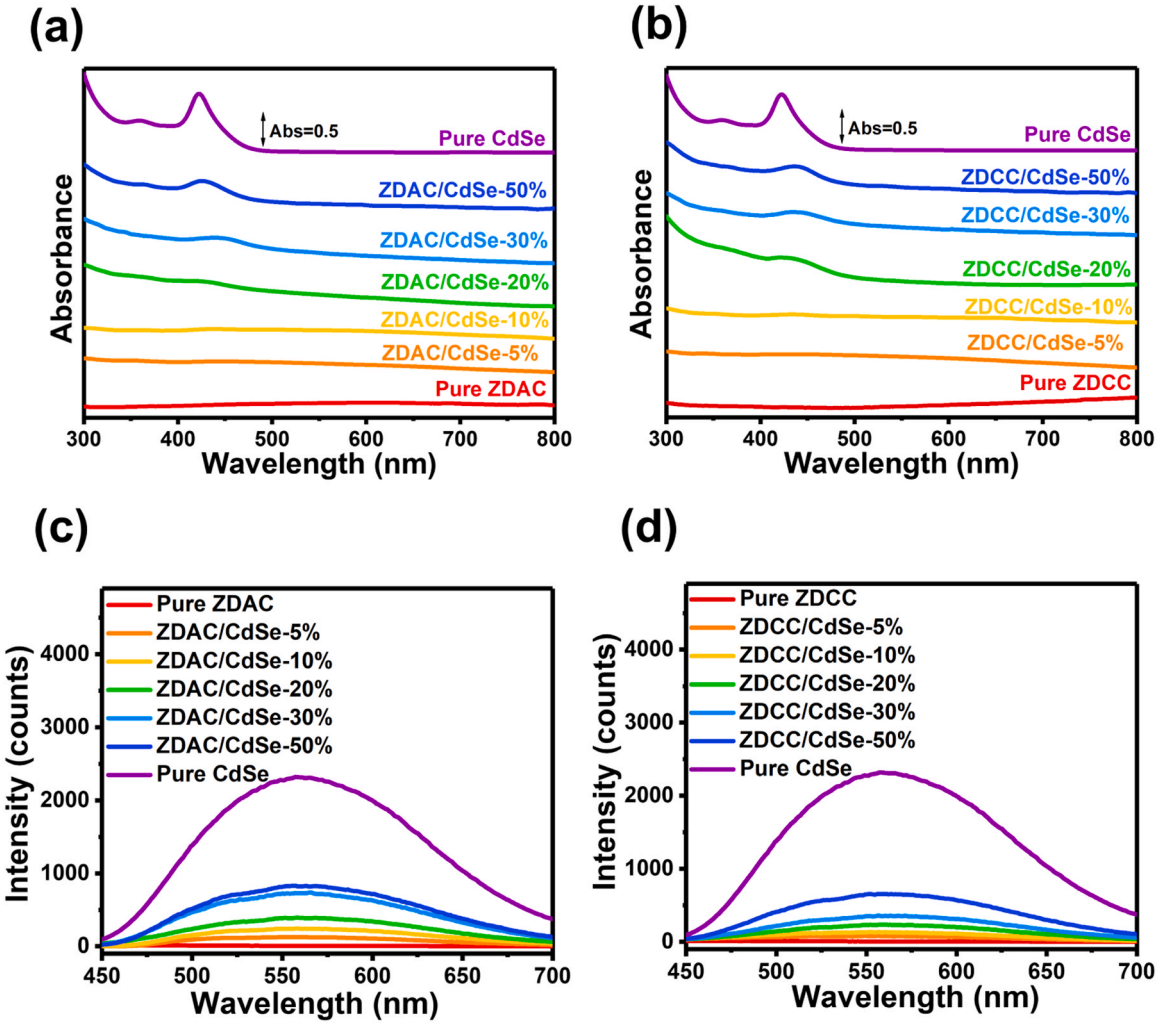

Fig. 3. UV–visible absorption spectra of (a) ZDAC/CdSe, (b) ZDCC/CdSe. Scales at absorbance are linear. Steady-state PL spectra of (c) ZDAC/CdSe, (d) ZDCC/CdSe. The data of pure CdSe, pure ZDAC, and pure ZDCC were also present for comparison.

of charge separation, a crucial factor contributing to improved photocatalytic performance. These results underscore the effective interaction between the MOF-derived carbons and CdSe in promoting interfacial charge transfer.

To investigate charge transfer dynamics, time-resolved PL measurements were conducted. Fig. 4(a-b) presents the PL decay profiles of the composites, with signals collected from photons emitted by the CdSe component. Comparison of the decay kinetics between pure CdSe and ZDAC/CdSe, and between pure CdSe and ZDCC/CdSe) provided both qualitative and quantitative insights into the impact of ZDAC and ZDCC on the charge transfer dynamics of CdSe. Notably, ZDCC/CdSe exhibited more pronounced PL decay kinetics compared to ZDAC/CdSe, indicating that ZDCC enhanced charge separation in CdSe more effectively than ZDAC. The decay curves were fitted to a bi-exponential equation to distinguish radiative (slow lifetime, τ_1) and nonradiative (fast lifetime, τ_2) relaxation pathways, with the intensity-average lifetime ($<\tau>$) computed to offer a comprehensive perspective [42]. As shown in Tables S1 and S2 (supplementary material), both ZDAC/CdSe and ZDCC/CdSe displayed significantly reduced average lifetimes compared to pure CdSe, reflecting improved charge separation efficiency in the composites. Comparative analysis revealed that ZDCC/CdSe achieved a greater reduction in carrier lifetime than ZDAC/CdSe, with ZDCC/CdSe-20 % demonstrating the shortest carrier lifetime among the tested concentrations. This finding indicates the highest level of charge separation for ZDCC/CdSe-20 %. Enhanced charge separation facilitates rapid interfacial charge transfer within the samples, which is critical for optimizing photocatalytic efficiency.

To further interrogate excited-state dynamics, fs-TA was performed on three representative samples, i.e., pure CdSe, ZDCC/CdSe-20 %, and ZDAC/CdSe-10 %. Measurements were conducted with 325 nm excitation while monitoring 350–700 nm. As shown in Fig. S10 (supplementary material), all samples exhibit a ground-state bleach (GSB) attributable to the 1S(e)–1$S_{3/2}$(h) transition, together with excited-state absorption features assigned to photoinduced carrier absorption from surface states [59–62]. Here, GSB originates from the deactivation of excited states upon irradiation. Tracking the temporal recovery of the GSB can thus deliver quantitative information regarding the excited-state dynamics of CdSe. In Fig. S11 (supplementary material), the kinetics profiles of GSB recovery at its minimum for the three samples are compared to examine the influence of ZDCC/ZDAC integration on the excited-state dynamics of CdSe. As summarized in Table S3 (supplementary material), the GSB recovery of pure CdSe can be described by tri-exponential kinetics, reflecting the multi-channel nature of carrier relaxation and recombination in CdSe. The first is a

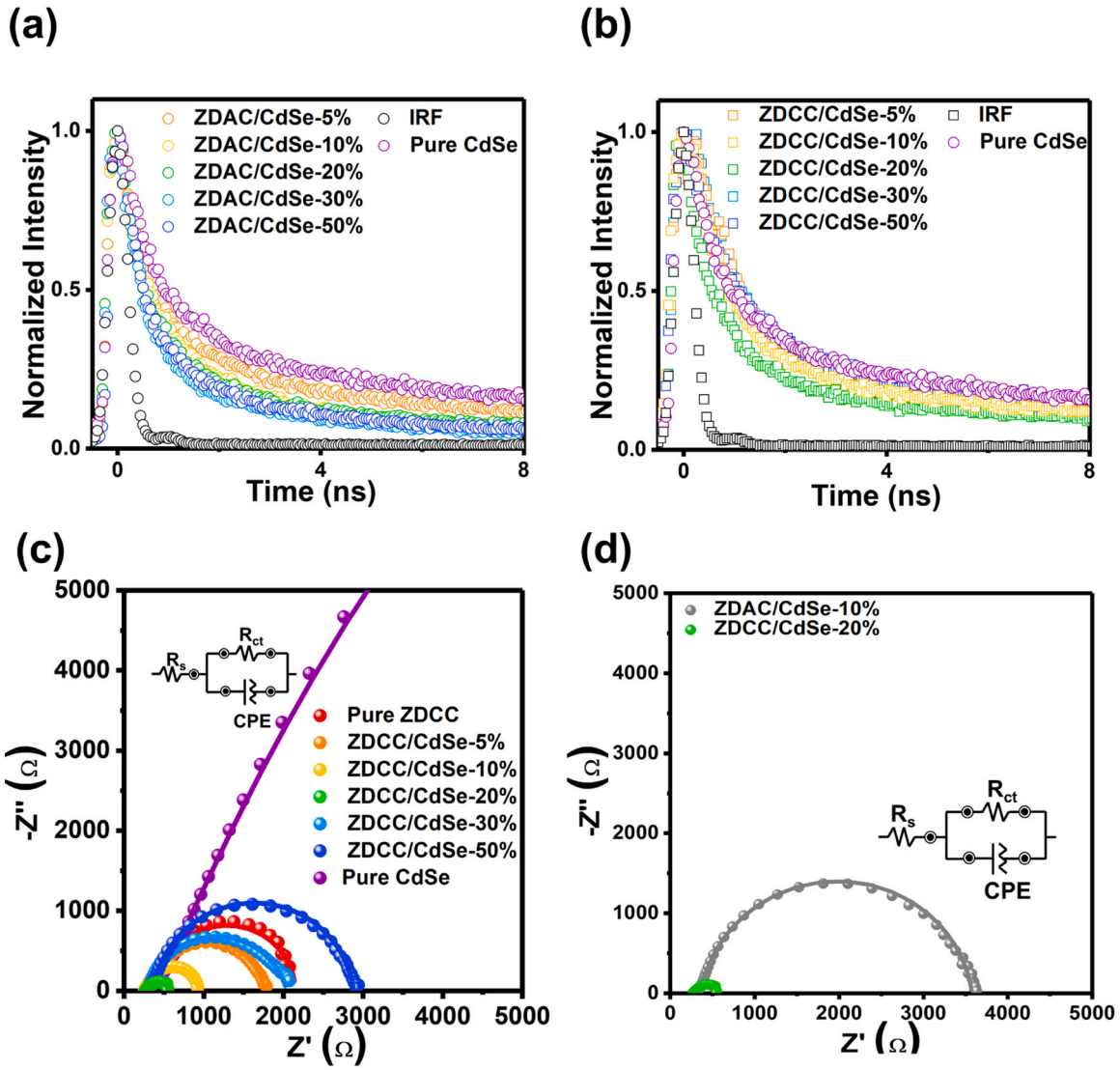

Fig. 4. Time-resolved PL spectra for (a) ZDAC/CdSe, (b) ZDCC/CdSe. The results of pure CdSe and IRF were also included. Nyquist plots for (c) pure CdSe, pure ZDCC, and ZDCC/CdSe, (d) ZDCC/CdSe-20 % and ZDAC/CdSe-10 %.

sub-ps component with $\tau_1 = 0.7$ ps and $A_1 = 0.18$, which may result from Auger recombination of electrons or holes, or from electronic transition at surface states. The second is a ps component with $\tau_2 = 16.5$ ps and $A_2 = 0.29$, which is associated with electronic transitions at trap states caused by defects. The third is a predominant ns component with $\tau_3 = 4.7$ ns and $A_3 = 0.53$, corresponding to band-to-band recombination. Relative to CdSe, both ZDCC/CdSe-20 % and ZDAC/CdSe-10 % display accelerated GSB recovery kinetics, consistent with the opening of an interfacial charge transfer pathway that expedites excited-state deactivation. The extracted lifetime components are $\tau_1 = 0.9$ ps ($A_1 = 0.78$), $\tau_2 = 42.7$ ps ($A_2 = 0.14$) and $\tau_3 = 3.0$ ns ($A_3 = 0.08$) for ZDCC/CdSe-20 %, and $\tau_1 = 0.9$ ps ($A_1 = 0.73$), $\tau_2 = 42.7$ ps ($A_2 = 0.16$) and $\tau_3 = 3.0$ ns ($A_3 = 0.11$) for ZDAC/CdSe-10 %. Noticeably, the amplitude of the ns component is substantially reduced in ZDCC/CdSe-20 % ($A_3 = 0.08$) and ZDAC/CdSe-10 % ($A_3 = 0.11$) relative to pure CdSe ($A_3 = 0.53$), signifying that integration of ZDCC or ZDAC markedly suppresses charge recombination in CdSe. This result is fundamentally consistent with the time-resolved PL data. Both datasets are qualitatively consistent in showing that the two composites enhance charge separation relative to pure CdSe. It should be emphasized that fs-TA and time-resolved PL primarily report on dynamics from sub-ps to ns, encompassing recombination, trapping, and interband and intraband relaxation. These are not the sole determinants of overall H_2 production. Processes on longer timescales, e.g., charge transfer to surface sites at μs-ms range, light harvesting efficiency, and surface reaction kinetics, also shape the observed activity. Overall, the combined analysis of time-resolved PL and fs-TA provides valuable mechanistic insight into early-time excited-state dynamics, but should be interpreted alongside these additional factors to fully rationalize the photocatalytic behavior.

In addition to interfacial charge transfer within the samples, charge transfer at the sample surface, particularly from the surface to the electrolyte, plays a critical role in determining overall photocatalytic performance. To assess surface charge transfer in ZDCC/CdSe-20 %, EIS analysis was performed at open circuit potential under AM 1.5 G illumination to measure the charge transfer resistance at the sample/electrolyte interface. The samples tested included pure CdSe, pure ZDCC, ZDCC/CdSe, and ZDAC/CdSe. Fig. 4(c) shows the Nyquist plots of relevant samples, which exhibited distinct semi-circular features. The equivalent circuit used for analysis included series resistance (R_s), charge transfer resistance (R_{ct}) at the sample/electrolyte interface, and a capacitance phase element (CPE). As summarized in Table S4 (supplementary material), ZDCC/CdSe demonstrated a decrease in R_{ct} with increasing CdSe concentration, reaching the lowest value of 0.27 kΩ for ZDCC/CdSe-20 %. Beyond this concentration, R_{ct} increased, indicating an optimal CdSe concentration for minimizing surface charge transfer resistance. On the other hand, the R_s values remained consistent across all samples, likely due to uniform electrolyte composition and consistent experimental conditions during measurements. The CPE, related to surface state capacitance, reflects surface carrier density, with higher values indicating a larger density of charge carriers [63,64]. Notably, ZDCC/CdSe-20 % exhibited the highest CPE, suggesting it contained the most abundant surface charge carriers, which may enhance its photocatalytic activity. This was further supported by comparative analysis in Fig. 4(d), where ZDCC/CdSe-20 % demonstrated superior charge transfer mobility compared to ZDAC/CdSe-10 %. This result aligns with the time-resolved PL data, showing that ZDCC facilitated more efficient charge separation and interfacial charge transfer than ZDAC. Here, the reduced surface charge transfer resistance in ZDCC/CdSe-20 % supports rapid charge carrier transfer to the reaction sites, minimizing recombination losses and promoting photocatalytic activity.

3.3. H_2 Production and practical applications

The photocatalytic performance was evaluated through H_2 production experiments under simulated solar irradiation, with the comparative results displayed in Fig. 5(a-b). The error bars added to the photocatalytic performance data are based on three independent replicates. Their small magnitude attests to the reproducibility and reliability of the results. All of the pure samples exhibited relatively low H_2 production activity, indicative of the limited carrier utilization efficiency typical of single-component materials. Pure ZDAC demonstrated significantly lower photocatalytic activity than pure ZDCC, primarily due to its poor ability to generate photoexcited charge carriers. Note that ZDAC was composed of metallic Co and amorphous carbons, which are non-responsive to light irradiation. In contrast, ZDCC, comprising CND, COS, and Co_3O_4, exhibited notable photoresponsive features [65–68]. The photoresponsive nature of its components, combined with the possible band alignment among Co_3O_4, CND, and COS, likely facilitated effective interfacial charge transfer, enhancing its performance. Coupling ZDAC and ZDCC with CdSe significantly improved H_2 production yields, with each composite showing an optimal CdSe loading concentration for maximum activity. ZDCC/CdSe outperformed ZDAC/CdSe under identical conditions, achieving H_2 production yields approximately seven times higher. This underscores the superior synergy between ZDCC and CdSe compared to ZDAC and CdSe. The long-term stability tests, shown in Fig. 5(c), confirmed the durability of ZDCC/CdSe-20 %, maintaining consistent H_2 production activity over 45 h. Furthermore, to evaluate the structural robustness of ZDCC/CdSe after prolonged operation, SEM, TEM, and XRD characterizations were performed on the sample before and after 45 h of solar H_2 production. The comparative results shown in Fig. S12 (supplementary material) confirm that the microstructure and crystallographic phase of ZDCC/CdSe remained well preserved, indicating high structural robustness under long-term photocatalytic operation.

The robust photocatalytic performance of ZDCC/CdSe suggests that the common issue of CdSe photocorrosion can be effectively mitigated. This improvement is likely attributed to a vectorial charge transfer mechanism, where photogenerated holes in CdSe recombine with photoexcited electrons in ZDCC. This Z-scheme charge transfer effectively removes photogenerated holes, preventing oxidative photocorrosion of the CdSe component [11,43] and contributing to the remarkable durability. Site-selective photodeposition experiments will further confirm this charge transfer mechanism. In Fig. 5(d), the AQY of H_2 production was measured across samples, revealing several notable features. First, pure CdSe exhibited activity under UV and visible light, with a maximum AQY of 2.7 % at 420 nm, but became inactive beyond its band gap excitation ($\lambda > 500$ nm) due to an inability to harvest photons. In contrast, pure ZDCC displayed activity across a broader range, from UV to NIR, due to multiple electronic transitions, including n-π* transitions in carbonyl bonds (UV region) [69,70] and ligand-metal charge transfer (visible region) [68,71,72] as revealed in Fig. S13 (supplementary material). ZDCC/CdSe-20 % demonstrated superior AQY across all tested wavelengths, reaching 6.4 % at 420 nm and 3.9 % at 800 nm, significantly outperforming pure CdSe and pure ZDCC. Notably, this performance was achieved without co-catalysts, suggesting that the addition of suitable co-catalysts could further enhance AQY. The strong synergy between ZDCC and CdSe, promoting efficient interfacial charge transfer, was key to this notable performance. Moreover, ZDCC/CdSe-20 % exhibited significant activity in the NIR range (λ = 600–800 nm), where CdSe-based photocatalysts are typically inactive. Table S5 (supplementary material) provides a comparative summary of the solar H_2 production performance of state-of-the-art CdSe-based photocatalysts reported in the literature. Most previously reported CdSe photocatalysts demonstrate activity only within their band gap absorption range, typically limited to wavelengths below 600 nm. Beyond this range, these photocatalysts exhibit negligible H_2 production activity. In contrast, the current ZDCC/CdSe composite achieves an unprecedented AQY of 3.9 % at 800 nm, marking a significant breakthrough. Only a few photocatalysts reported to date have demonstrated activity under NIR irradiation [73–75]. This unique NIR-responsive capability allows ZDCC/CdSe to address a critical gap by effectively harvesting

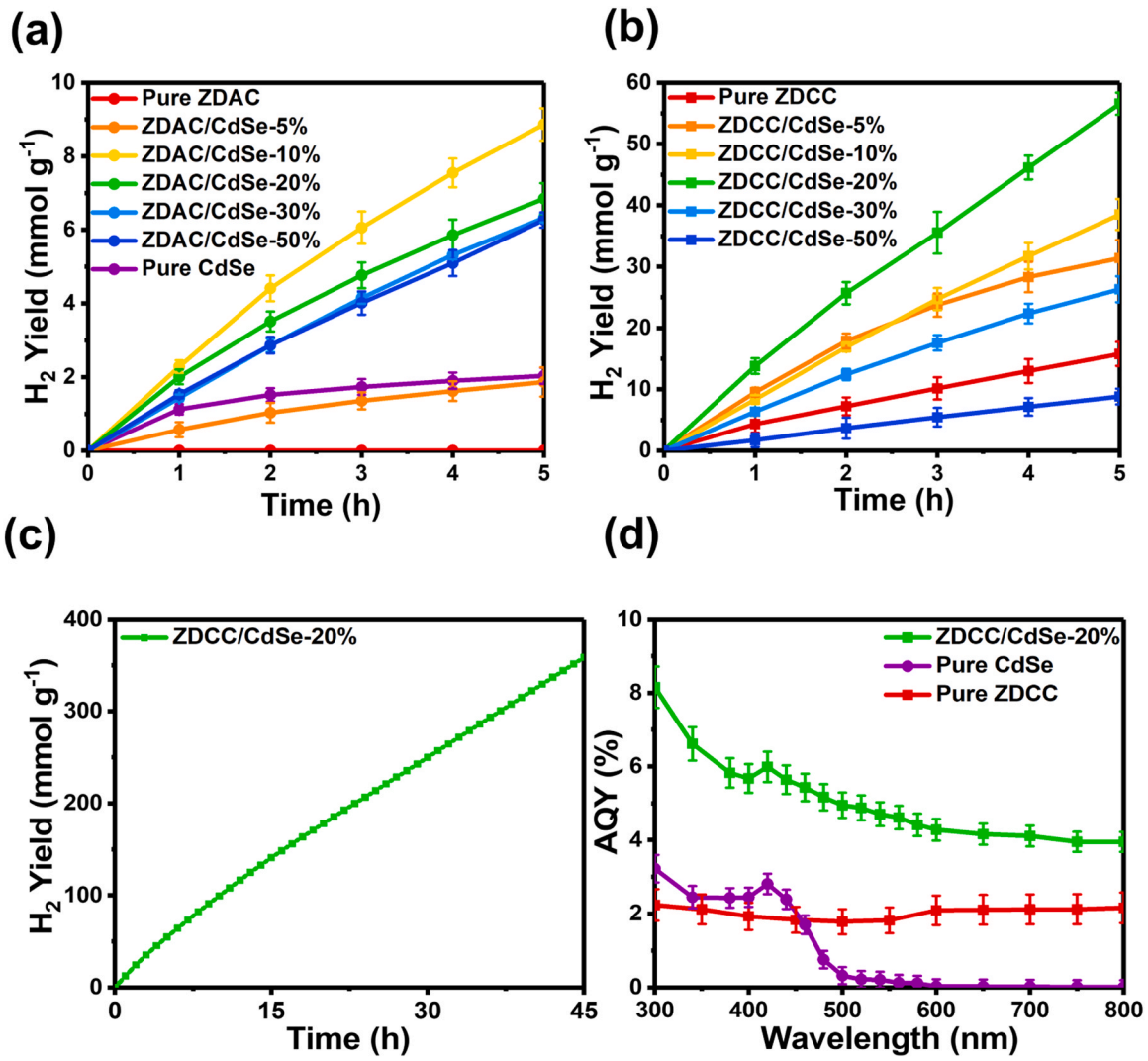

Fig. 5. Time-dependent solar H_2 production data for (a) ZDAC/CdSe, (b) ZDCC/CdSe with various CdSe concentrations. (c) Long-term stability tests of solar H_2 production on ZDCC/CdSe-20 %. (d) Distribution of AQY values for pure CdSe, pure ZDCC, and ZDCC/CdSe-20 %.

untapped NIR energy for solar H_2 production, offering a promising pathway for enhanced utilization of the solar spectrum. To assess the potential scattering effect, the internal quantum yield (IQY) was calculated by normalizing the AQY to the absorbance (A) at the corresponding wavelength using Equation S2 (supplementary material). The difference between IQY and AQY quantifies optical-access losses arising from scattering and reflectance. As shown in Fig. S24, deviations were observed (0.07 % at 400 nm, 0.07 % at 600 nm, 0.06 % at 800 nm), indicating non-negligible scattering and reflectance for the large-sized ZDCC/CdSe. Nevertheless, this gap is actionable. Optimizing the optical path to unity and enhancing photon re-collection through reactor design can credibly reduce these losses. To illustrate its practical potential, H_2 produced by ZDCC/CdSe-20 % under 24 h of AM 1.5 G irradiation was used to power a fuel cell, generating 5.68 mW to operate a motorized mini fan continuously for 20 sec. As Video S1 (supplementary material) displays, this demonstration underscores the capability of ZDCC/CdSe as a highly effective photocatalyst for sustainable H_2 production and its applicability in powering electric devices. To assess the energy-conversion performance of this system, the apparent solar-to-hydrogen (STH) efficiency based on the Gibbs free energy change of the actual net reaction occurring in the system, namely the oxidation of *L*-ascorbic acid coupled with proton reduction, was evaluated. The calculations were detailed in the supplementary material. The apparent STH values of ZDCC/CdSe-20 %, pure ZDCC, and pure CdSe were determined to be 0.18 %, 0.03 %, and 0.007 %, respectively.

3.4. Photocatalytic mechanism

The photocatalytic mechanism of ZDCC/CdSe was elucidated by determining the band structure of its components using UPS. As shown in Fig. S14 (supplementary material), the secondary-electron cut-off regions revealed cut-off energies of 16.91 eV for ZDCC and 18.12 eV for CdSe. Subtracting these values from the incident photon energy (21.22 eV) [76] yielded work function values of 4.31 eV for ZDCC and 3.10 eV for CdSe. The valence band maximum (E_{VB}) relative to the Fermi level (E_F) was calculated by linear extrapolation, resulting in ($E_{VB} - E_F$) values of 2.33 eV for ZDCC and 2.31 eV for CdSe. Adding the work function values gave E_{VB} values of −6.64 eV for ZDCC and −5.41 eV for CdSe relative to the vacuum level. The conduction band minimum (E_{CB}) was then determined by adding the optical band gap values derived from Fig. S13 and S15 (supplementary material) (2.92 eV for ZDCC and 2.77 eV for CdSe), yielding E_{CB} values of −3.72 eV for ZDCC and −2.64 eV for CdSe. Note that the size-dependent band gap of zinc blende CdSe quantum dots can be quantitatively described by Equation S3 (supplementary material). In this work, the average particle size of pure CdSe is measured to be 1.83 ± 0.23 nm, and the observed optical band gap is 2.77 eV. Substituting the experimentally measured particle size (d = 1.83 nm) into the empirical relation yields E_g = 2.78 eV, in good

agreement with the experimentally determined optical band gap. This consistency underscores the reliability of the observed optical band gap, further validating the proposed band structure model. The resulting band structure of ZDCC/CdSe was depicted in Fig. 6(a). Note that the energetic levels of E_{VB}, E_{CB}, and E_F were represented against the normal hydrogen electrode (NHE) to offer a more insightful thermodynamics viewpoint. Because of the E_F alignment, band bending was expected to occur at the interface of ZDCC/CdSe. The band bending and E_F alignment can be clarified by examining the electronic interactions at the ZDCC/CdSe interface. To probe these interactions, XPS spectra of ZDCC/CdSe were compared with those of pure ZDCC and pure CdSe. The comparative results of Fig. S16(a-d) (supplementary material) clearly reveal binding energy shifts between the composite sample and pure components. For ZDCC/CdSe, the binding energies of Co 2p and C 1 s were lower than those of pure ZDCC, while the binding energies of Cd 3d and Se 3d were higher than those of pure CdSe. This complementary binding energy shift suggests electron transfer from CdSe to ZDCC occurred upon their contact. This electron transfer pathway is induced by the alignment of E_F between CdSe and ZDCC. As shown in Fig. S16(e), as CdSe is put in contact with ZDCC, the higher E_F of CdSe than that of ZDCC induces interfacial electron transfer from CdSe to ZDCC until their E_F values are equilibrated. The alignment of E_F would create band bending at the interface, which further dictates the charge transfer scenario under light illumination, as depicted in Fig. 6(a). As Fig. 6(a) shows, the downward band bending at the conduction band of ZDCC and the upward band bending at the valence band of CdSe can steer charge transfer dynamics following a direct Z-scheme mechanism [77,78]. Under light illumination, the photoexcited electrons of ZDCC recombine with the photogenerated holes of CdSe, spatially separating the remaining charge carriers by leaving electrons in the conduction band of CdSe and holes in the valence band of ZDCC. The site-selective photodeposition experiments further validated this mechanism. As shown in Fig. 6(b) and Fig. S17 (supplementary material), Pt particles were selectively deposited on the CdSe surface of ZDCC/CdSe, confirming the accumulation of photoexcited electrons in CdSe. Conversely, PbO_2 was primarily deposited on the ZDCC region, as revealed in Fig. 6(c) and Fig. S18 (supplementary material), indicating that photogenerated holes were concentrated in ZDCC. These findings conclusively demonstrated the direct Z-scheme charge transfer pathway in ZDCC/CdSe. This mechanism underpins the robust photocatalytic performance of ZDCC/CdSe. By efficiently removing photogenerated holes from CdSe via recombination with the photoexcited electrons of ZDCC, oxidative photocorrosion of CdSe is mitigated, ensuring the durability of ZDCC/CdSe in solar H_2 production applications.

To further validate the proposed charge transfer mechanism under real irradiation conditions, in-situ XAS was conducted under AM 1.5 G illumination. XAS spectra of ZDCC/CdSe-20 % were obtained both in darkness and under illumination, enabling the analysis of changes in the unoccupied density of states (UDOS) resulting from light exposure. The absorption difference (ΔA) spectrum was calculated as ($\Delta A = A_{light} -$

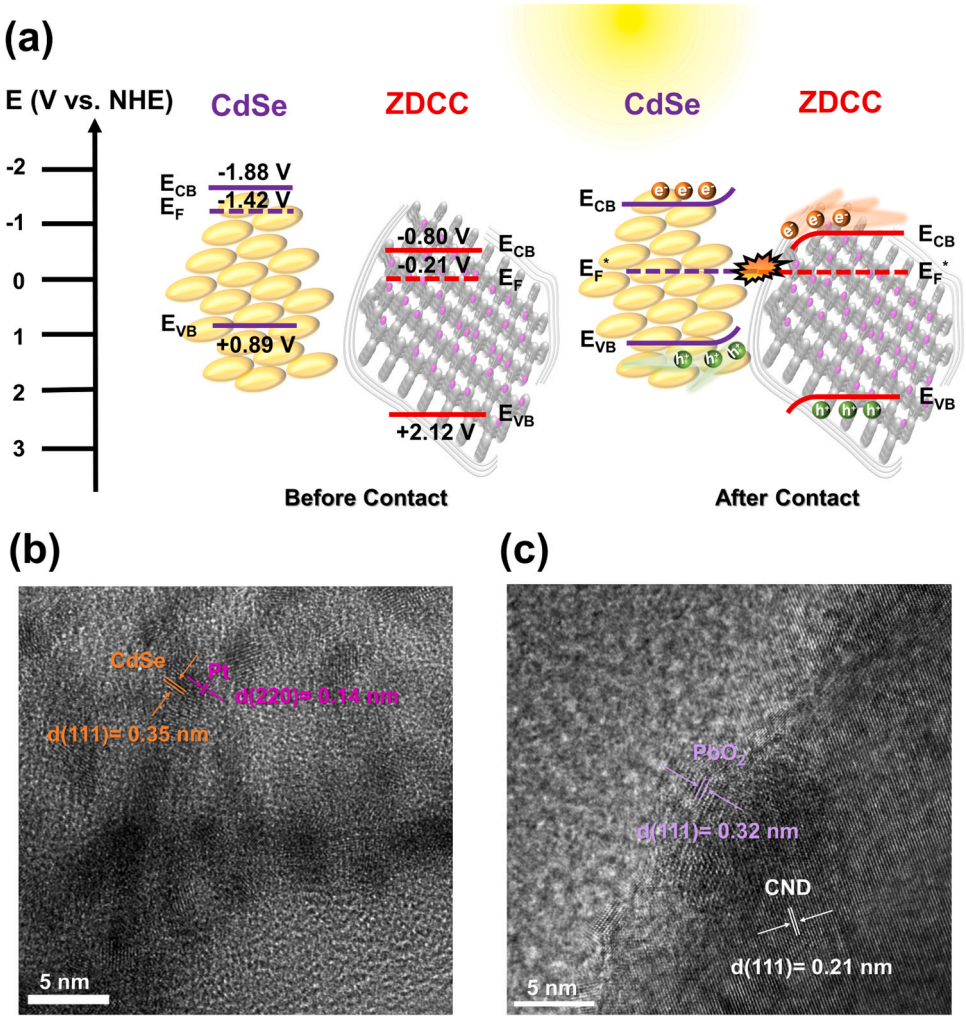

Fig. 6. (a) Calculated band structure for ZDCC/CdSe and proposed charge transfer scenario for ZDCC/CdSe under light illumination. TEM images for ZDCC/CdSe-20 % upon selective photodeposition of (b) Pt and (c) PbO_2.

A_{dark}) [76,79], providing both qualitative and quantitative insights into the charge transfer pathways induced by light. Fig. 7(a) presents the Co K-edge spectra of ZDCC/CdSe-20 %. Under illumination, a significant increase in the Co K-edge intensity was observed, resulting in a positive ΔA spectrum with an area of + 0.14. This increase in UDOS is indicative of electron depletion in the ZDCC component. This finding is consistent with the proposed direct Z-scheme mechanism, in which photoexcited electrons in ZDCC recombine with photogenerated holes in CdSe. The vectorial charge transfer process causes electron depletion in ZDCC, explaining the positive ΔA observed in the Co K-edge spectrum. Further complementary evidence was provided by the Cd K-edge spectrum, displayed in Fig. 7(b). Upon illumination, the Cd K-edge intensity decreased significantly, producing a negative ΔA area of −0.35. This decrease reflects electron accumulation in the CdSe component of ZDCC/CdSe, supporting the proposed charge transfer scenario. These in-situ XAS findings confirm the validity of the direct Z-scheme charge transfer mechanism for ZDCC/CdSe under actual irradiation conditions. The vectorial charge transfer at the interface effectively separates charge carriers, with photoexcited electrons retained in the conduction band of CdSe and photogenerated holes confined to the valence band of ZDCC. This spatial separation of charge carriers prolongs their lifetimes, enabling more efficient participation in surface redox reactions. Such processes are critical for the enhanced photocatalytic performance observed in ZDCC/CdSe composites.

To investigate the behavior of charge carriers at the sample surface, μs-TA spectroscopy measurements were performed. It is important to note that charge transfer and recombination within the bulk of photocatalysts generally occur on ultrafast timescales (fs to ns) [80], whereas charge migration and transfer at the photocatalyst/electrolyte interface take place over longer timescales (μs to ms) [81]. Since surface redox reactions are the rate-limiting steps in photocatalysis, analyzing charge transfer dynamics at the sample surface on these longer timescales provides critical insights into photocatalytic performance. Fig. 7(c) presents an analysis of TA spectral features for ZDCC/CdSe-20 % and pure CdSe under two experimental conditions: without an electron scavenger and in the presence of an electron scavenger. In the absence of an electron scavenger, both ZDCC/CdSe-20 % and pure CdSe exhibited negative TA signals in the 600–800 nm range upon photoexcitation. These signals were rapidly bleached due to the deactivation of photoexcited charge carriers. The TA spectra were also recorded in the

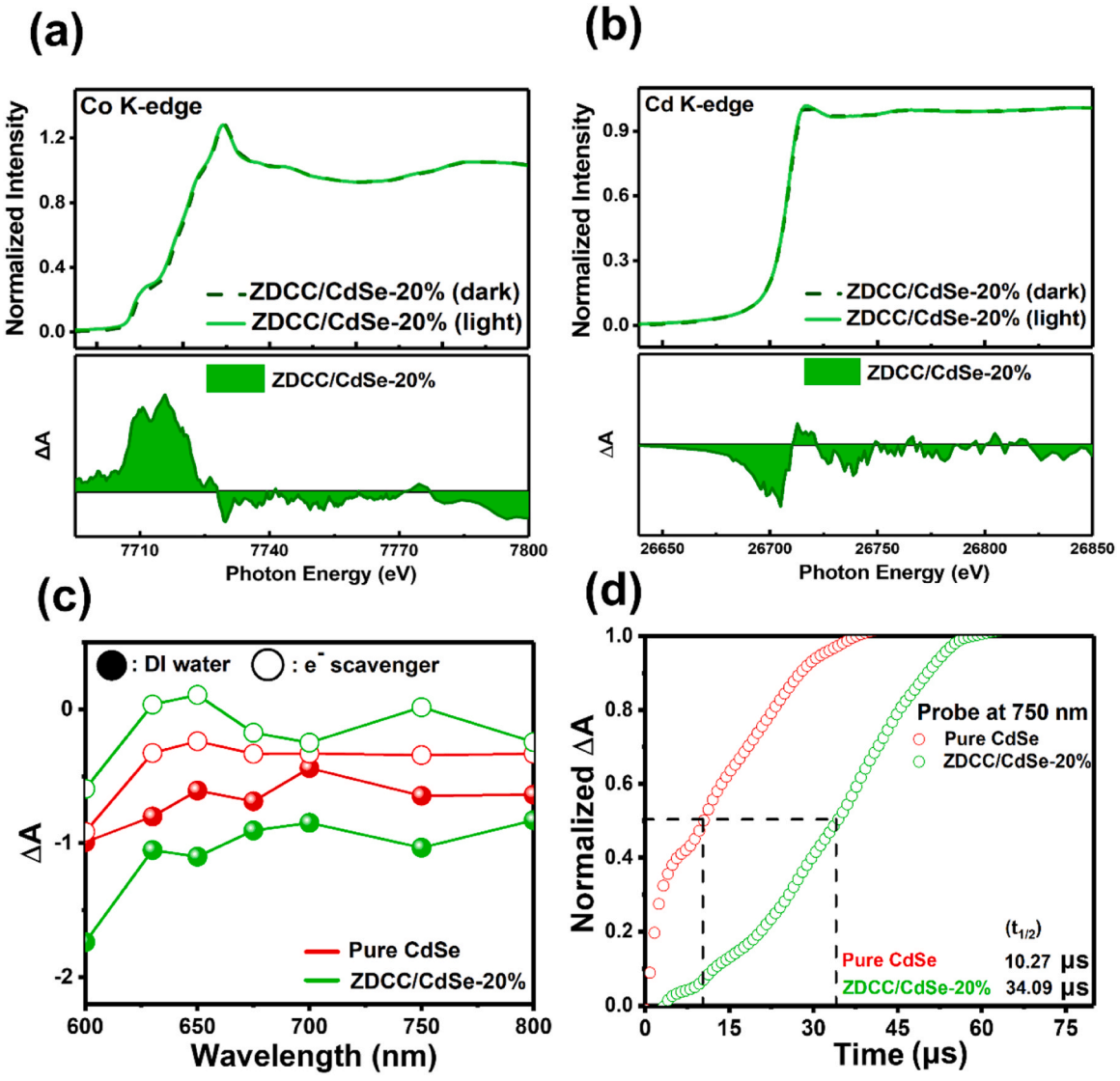

Fig. 7. XAS spectra of ZDCC/CdSe-20 % recorded under darkness and irradiation conditions and the corresponding intensity difference profiles: (a) Co K-edge spectra, (b) Cd K-edge spectra. (c) TA spectra recorded using a pump wavelength of 390 nm without an electron scavenger (DI water) and in the presence of an electron scavenger: at a delay time of 5 μs for ZDCC/CdSe-20 % and pure CdSe. (d) Kinetic traces at 750 nm from TA spectra recorded in the electrolyte (0.5 M *L*-ascorbic acid) for ZDCC/CdSe-20 % and pure CdSe.

presence of an electron scavenger to isolate and analyze the kinetic signals of delocalized electrons at the sample surface. Upon introducing the electron scavenger, a significant reduction in TA intensity was observed for both ZDCC/CdSe-20 % and pure CdSe. This reduction is consistent with the expected capture of delocalized electrons by the scavenger, which effectively removes these electrons from the sample surface. The TA signal at 750 nm was attributed to delocalized surface electrons in CdSe, aligning with previous reports that identified TA kinetics of hydrated or solvent electrons in CdSe primarily in the red to NIR region [81–83]. To further examine the behavior of these delocalized electrons under photocatalytic reaction conditions, μs-TA measurements were performed in the electrolyte (0.5 M *L*-ascorbic acid), and the resulting kinetic traces at 750 nm were analyzed. As shown in Fig. 7(d), pure CdSe exhibited a rapid decay of delocalized electron kinetics with a half-life ($\tau_{1/2}$) of 10.27 μs. In contrast, ZDCC/CdSe-20 % displayed significantly prolonged decay kinetics, with a $\tau_{1/2}$ of 34.09 μs. This result aligns with the proposed Z-scheme charge transfer mechanism illustrated in Fig. 6(a). Upon light irradiation, vectorial charge transfer at the interface spatially separates photoexcited electrons in CdSe from photogenerated holes in ZDCC. The delocalized electrons of CdSe would readily diffuse to the sample surface, surviving for an extended time to prolong the TA decay kinetics for ZDCC/CdSe. These TA analytical results provide compelling evidence that ZDCC effectively modifies charge transfer dynamics at the surface of CdSe, enhancing electron lifetime and promoting photocatalytic performance for H_2 production.

The origin of the superiority of ZDCC to ZDAC in photocatalytic performance can also be comprehended by Raman spectroscopy and EIS analysis. The distinct carbon structural features in ZDAC and ZDCC were first examined with Raman spectroscopy in Fig. S19 (supplementary material). Pure ZDAC displayed the characteristic D band and G band centered around 1350 cm^{-1} and 1580 cm^{-1}, respectively, a spectral signature associated with amorphous carbons. Note that amorphous carbons typically exhibit both the D band and G band in the Raman spectrum owing to the presence of disordered sp^2-hybridized carbon structures. The G band arises from bond stretching of sp^2 carbon pairs in both aromatic rings and chains, while the D band originates from breathing modes of aromatic rings that are activated by disorder and finite crystallite size [84,85]. Pure ZDCC also exhibits two Raman peaks, while the recorded frequencies are substantially different from those of the typical D band and G band. The prominent peak centered at 1325 cm^{-1} is a signature of sp^3-hybridized nanodiamond structures. This peak is assigned to the first-order transverse optical phonon mode of the cubic diamond lattice, and represents the zone-center (Γ-point) phonon vibration [86,87]. The observed downshift and broadening of this peak, relative to the peak position of bulk diamond at 1332 cm^{-1}, are attributed to the phonon-confinement effect and lattice disorder within nanoscale crystallites. The other broad band near 1600–1640 cm^{-1} is likely due to O–H bending vibrations associated with the functional groups present at dangling bonds [86–88]. The analytical results of Raman spectroscopy confirm the amorphous carbon structure for ZDAC and the crystalline carbon structure for ZDCC. The implications of this carbon structural difference in charge transfer are further investigated by EIS analysis. Fig. S20 (supplementary material) compares the Nyquist plots for pure ZDAC and pure ZDCC, in which pure ZDCC exhibits a significantly smaller semicircular arc, signifying a lower charge transfer resistance in ZDCC. The composed crystalline carbons in ZDCC may facilitate charge carrier transfer, leading to the observed lower charge transfer resistance. Therefore, more effective carrier extraction and utilization are expected for pure ZDCC, which is beneficial for photocatalytic performance.

To elaborate on the above argument, μs-TA measurements were performed on pure ZDAC and pure ZDCC in the electrolyte used for the photocatalytic reaction (0.5 M *L*-ascorbic acid). The thus-collected charge dynamics data can reflect the kinetics of the surface charge carriers during their participation in H_2 production, providing spectroscopic evidence to elucidate the distinct roles of the carbon structure of ZDAC and ZDCC in photocatalysis. Fig. S21(a,b) (supplementary material) shows the comparative results of the μs-TA data. Upon 390 nm excitation, pure ZDCC displayed larger TA intensities than pure ZDAC from 350 to 800 nm at the same delay times. As carrier transportation is effective in ZDCC, the delocalized charge carriers in significant amounts can diffuse to the surface for further utilization, leading to the increased TA intensities for pure ZDCC. The kinetics traces were analyzed in Fig. S21(c) to obtain quantitative information on the fate of the surface charge carriers. Here, the temporal profiles were obtained by integrating the area under the TA spectral profiles from 350 to 800 nm in order to comprehend all of the involved surface charge carriers as an ensemble. Compared to pure ZDAC ($\tau_{1/2}$ = 11.56 μs), pure ZDCC exhibited prolonged decay kinetics of surface charge carriers with a $\tau_{1/2}$ of 16.74 μs. This outcome suggested that the surface charge carriers at ZDCC can survive longer than those at ZDAC during their participation in H_2 production. The relatively abundant and long-lived surface charge carriers may ensure efficient utilization in the subsequent H_2 production, which can explain the superior photocatalytic performance of ZDCC to ZDAC. These findings, collectively supported by Raman spectra and EIS analysis, confirm that the carbon structural features in ZDAC and ZDCC dictate charge transfer dynamics, therefore determining the overall photocatalytic performance.

The critical role of the Co center of ZDCC in enabling the high photocatalytic efficiency of ZDCC/CdSe was investigated in greater detail. To identify the function of the Co center of ZDCC, in-situ soft-XAS experiments were performed on ZDCC/CdSe under illumination in 0.5 M *L*-ascorbic acid to simulate photocatalytic operating conditions. In contrast to hard-XAS, which probes bulk features, soft-XAS is surface-sensitive and therefore well suited to resolving surface active sites relevant to catalysis. Here, soft-XAS was employed to measure Co L_3-edge spectra of ZDCC/CdSe-20 % under illumination. Two conditions were examined and compared: (i) the sample dispersed in DI water, an essentially inert electrolyte that yielded negligible H_2 and thus reported on photoexcited states without productive catalysis; and (ii) the sample dispersed in 0.5 M *L*-ascorbic acid, an active electrolyte that supported efficient H_2 production. Differences between these spectra reveal illumination-induced electronic-structure changes associated with catalytic turnover, providing direct insight into the catalytic role of Co centers in photocatalytic H_2 production. For Co L_3-edge absorption, the electronic transition arises from 2p core electrons excited to the partially filled 3d orbital, directly probing the valence shell of Co that is sensitive to charge states. In Fig. S22 (supplementary material), the recorded spectral features resembled those of Co_3O_4, characterized by a tetrahedral Co^{2+} site at 777.5 eV and an octahedral Co^{3+} site at 780.5 eV. [89] Relative to the spectrum acquired in DI water, the spectrum collected in *L*-ascorbic acid shows two notable changes: (i) enhanced low-energy absorption characteristic of Co^{2+} and (ii) diminished high-energy absorption associated with Co^{3+}. These features indicate partial reduction of surface Co centers and concomitant changes in the Co-O coordination environment, consistent with a shift from Co^{3+} to Co^{2+}. The resulting enrichment of surface Co^{2+} species appears crucial for enabling efficient photocatalytic H_2 production on ZDCC/CdSe. Notably, *L*-ascorbic acid serves not only as a hole scavenger but also as a chemical reductant capable of converting Co^{3+} to Co^{2+} [90] in the ZDCC component. This redox process concurrently generates protons that further promote H_2 production. Taken together, the in-situ Co L_3-edge observations identify the Co^{3+}/Co^{2+} redox couple in the ZDCC component as a key facilitator of photocatalytic H_2 production on ZDCC/CdSe.

To further highlight the indispensable function of the Co center of ZDCC, we have synthesized a counterpart sample by using ZIF-8, which shares the same framework structure as ZIF-67 but incorporates Zn^{2+} instead of Co^{2+}, and performed a comparative study. Upon pyrolysis under H_2, the resulting ZnDC exhibited significant differences in both microstructural features and photocatalytic performance. In Fig. S23(a) (supplementary material), HRTEM and SAED analysis confirmed the

formation of ZnO nanoparticles, presumably resulting from the rapid oxidation of the dispersed Zn in air. Unlike ZDCC, ZnDC was not characteristic of graphitic carbon features. The carbon matrix of ZnDC remained fully amorphous, suggesting that Zn is incapable of facilitating the transformation of organic ligands into highly ordered, crystalline carbons. This contrast result also highlights the crucial role of Co for promoting the structural reorganization of ZIF-67 during carbonization. The as-obtained ZnDC was further characterized with XRD and absorption spectroscopy. In Fig. S23(b), the XRD pattern did not show characteristic peaks of ZnO, probably due to the poor crystallinity and small particle size. In Fig. S23(c), the absorption spectrum exhibited a broad, featureless band extending to the UV region, indicating limited photon harvesting capability. The as-obtained ZnDC was also coupled with CdSe to examine the photocatalytic performance. Fig. S23(d) shows the comparative results of photocatalytic H_2 production on pure ZnDC, ZnDC/CdSe-20 %, pure ZDCC, and ZDCC/CdSe-20 %. Compared to the counterpart ZIF-67-derived samples, i.e., pure ZDCC and ZDCC/CdSe-20 %, pure ZnDC and ZnDC/CdS-20 % both displayed substantially lower H_2 production yields. These findings confirm that the Co center of ZIF-67 is not only crucial for constructing a crystalline, structurally ordered carbon matrix in the derived carbons, but also is adequate for achieving high photocatalytic activity. This demonstration is fundamentally consistent with the in-situ Co L_3-edge spectra, revealing that Co centers of ZDCC play a uniquely important role in promoting the photocatalytic H_2 production on CdSe.

3.5. Global performance comparison

It should be noted that CdSe is a prototypical visible-light photocatalyst owing to its relatively narrow band gap, but its absorption is largely confined to the visible region and it is prone to severe photocorrosion. To overcome these limitations, this study integrates ZIF-derived carbons with CdSe quantum dots. The resulting heterostructures extend the photoresponse from the visible into the NIR while simultaneously mitigating the photocorrosion of CdSe. Photothermal catalysis is an alternative route for broadening the operational spectrum of semiconductor photocatalysts. For CdSe, however, reports are scarce, likely because CdSe itself is a poor photothermal converter. Table S6 (supplementary material) summarizes two representative examples. In one study, $MoSe_2$ served as a photothermal agent, generating heat under irradiation. The thermal field was proposed to facilitate charge transfer in $MoSe_2$/CdSe composites, delivering an H_2 AQY of 27.2 % at 670 nm [91]. In another study, ZnSe/CdSe@N-doped carbon was applied to CO_2 reduction, where N-doped carbon provided photothermal heating. The resultant surface-temperature rise was suggested to enhance both charge transfer and molecular diffusion, achieving AQY of CO and CH_4 production of 0.441 % at 980 nm [92]. While effective, these strategies rely on externally induced thermal contributions. Disentangling thermal from purely photocatalytic (non-thermal) pathways is intrinsically challenging because local heating under illumination is heterogeneous at the nanoscale and difficult to quantify with precision. This ambiguity can complicate mechanistic assignment, hinder reproducibility across materials sets. Importantly, elevated temperatures do not address the root cause of photocorrosion of CdSe, accumulation of highly oxidizing holes at the surface, and may even accelerate degradation kinetics. By contrast, extending activity via a true light-absorber from heterostructures provides a mechanistic, testable pathway. The current ZDCC/CdSe heterostructure system achieves visible-to-NIR photoactivity without involving external photothermal effects and exhibits stable H_2 production for up to 45 h, underscoring a robust and defensible design strategy that clearly distinguishes this approach from conventional photothermal methods.

To further underscore the innovation of the current system, a comprehensive literature survey has been performed to compile a table of MOF-derived materials coupled with chalcogenides for photocatalytic applications. As summarized in Table S7 (supplementary material), ZIF-derived carbons integrated with CdSe as photocatalysts have not been reported, highlighting the novelty of materials design. Although Z-scheme charge transfer and H_2 production have been demonstrated in other heterostructures, none exhibit photocatalytic activity that extends into the NIR; most reports are confined to the visible range, with no performance documented at wavelengths beyond 600 nm. Leveraging the broad light absorption of ZIF-derived carbons, the current ZDCC/CdSe achieves remarkable H_2 production under both visible and NIR irradiation. To further underscore the superior performance of ZDCC/CdSe in global scenarios, an additional performance comparison was summarized in Table S8 (supplementary material), which compiles representative CdSe-based photoelectrochemical systems from the literature for context. It should be noticed that the current solar H_2 production system operates with powder suspensions under zero bias, fundamentally differing from photoelectrochemical cells that use electrodes under applied potential; direct, like-for-like benchmarking is therefore not feasible. Even so, the distinct advantage of ZDCC/CdSe is evident in its robust NIR activity without bias (AQY = 3.9 % at 800 nm). As highlighted in Table S8, only a few CdSe-based photoelectrodes report responses at $\lambda > 600$ nm, for example, CdSe/CdS/ZnO/TiO_2 (7 % incident photon-to-current efficiency at 700 nm) and CdSe/CeO_2/Au (5 % incident photon-to-current efficiency at 700 nm), and these values are achieved under applied bias. By contrast, the unbiased AQY of 3.9 % at 800 nm reflects the intrinsic materials advantages of ZDCC/CdSe for solar H_2 production. Furthermore, a side-by-side comparison with state-of-the-art CdSe-based photocatalysts (Table S5) underscores the superior capability of the current system to harness the previously underutilized NIR portion of the solar spectrum. Collectively, these data emphasize both the innovative character and the performance advantages of ZDCC/CdSe for solar H_2 production.

4. Conclusions

The integration of MOF-derived carbons with CdSe quantum dots represents a synergistic strategy for addressing the dual challenges of efficiency and stability in solar H_2 production. The ZDCC/CdSe composite leverages a direct Z-scheme charge transfer mechanism, effectively optimizing the harnessing and spatial separation of charge carriers. This mechanism significantly enhances photocatalytic performance while ensuring durability, marking a substantial advancement in the field of solar H_2 production. Notably, ZDCC/CdSe exhibited notable activity in the NIR region, bridging a critical gap in the utilization of the solar spectrum. This breakthrough expands the operational wavelength range of CdSe-based photocatalysts, enabling more comprehensive harvesting of solar energy. Furthermore, the practical applicability of ZDCC/CdSe was demonstrated through its ability to generate H_2, which was subsequently used to produce electricity and power a motorized mini fan. This real-world demonstration highlights its potential for integration into sustainable energy systems. These findings pave the way for the development of next-generation photocatalysts that emphasize environmental sustainability, energy efficiency, and broader spectral responsiveness.

CRediT authorship contribution statement

Chien-Yi Wang: Conceptualization, Methodology, Validation, Formal analysis, Investigation, Writing - Original Draft. **Yu-Chen Wei:** Validation, Formal analysis, Investigation. **Yu-Chang Lin:** Validation, Formal analysis, Investigation. **Sudhakar Narra:** Validation, Formal analysis, Investigation. **Chun-Yi Chen:** Conceptualization, Methodology, Validation. **Tso-Fu Mark Chang:** Conceptualization, Methodology, Validation. **Masato Sone:** Conceptualization, Methodology, Validation. **Ying-Chih Pu:** Conceptualization, Methodology, Validation. **Eric Wei-Guang Diau:** Conceptualization, Methodology, Validation. **Yan-Gu Lin:** Conceptualization, Methodology, Validation, Resources, Supervision. **Cheng-Yu Wang:** Conceptualization, Methodology, Validation,

Resources, Supervision. **Yung-Jung Hsu:** Conceptualization, Methodology, Validation, Resources, Writing - Review & Editing, Visualization, Supervision, Project administration, Funding acquisition.

Declaration of Competing Interest

The authors declare that they have no known competing financial interests or personal relationships that could have appeared to influence the work reported in this paper.

Acknowledgements

This work was financially supported by the National Science and Technology Council, Taiwan, under grants MOST 111–2628-E-A49-001-MY3, NSTC 112–2221-E-A49-035-MY2, NSTC 114–2221-E-A49-109-MY3, NSTC 112–2113-M-A49–024 and NSTC 113–2113-M-A49–026. This work was also supported by the Center for Emergent Functional Matter Science of National Yang Ming Chiao Tung University from The Featured Areas Research Center Program within the framework of the Higher Education Sprout Project by the Ministry of Education (MOE) in Taiwan.

Appendix A. Supporting information

Supplementary data associated with this article can be found in the online version at doi:10.1016/j.apcatb.2026.126552.

Data availability

Data will be made available on request.

References

[1] H. Song, S. Luo, H. Huang, B. Deng, J. Ye, Solar-driven hydrogen production: recent advances, challenges, and future perspectives, ACS Energy Lett. 7 (2022) 1043–1065, https://doi.org/10.1021/acsenergylett.1c02591.
[2] K.C. Christoforidis, P. Fornasiero, Photocatalytic hydrogen production: a rift into the future energy supply, ChemCatChem 9 (2017) 1523–1544, https://doi.org/10.1002/cctc.201601659.
[3] P.Y. Hsieh, T. Kameyama, T. Takiyama, K. Masuoka, T. Yamamoto, Y.J. Hsu, T. Torimoto, Controlling the visible-light driven photocatalytic activity of alloyed ZnSe–AgInSe2 quantum dots for hydrogen production, J. Mater. Chem. A. 8 (2020) 13142–13149, https://doi.org/10.1039/D0TA04127K.
[4] Y.H. Chiu, S.B. Naghadeh, S.A. Lindley, T.H. Lai, M.Y. Kuo, K.D. Chang, J.Z. Zhang, Y.J. Hsu, Yolk-shell nanostructures as an emerging photocatalyst paradigm for solar hydrogen generation, Nano Energy 62 (2019) 289–298, https://doi.org/10.1016/j.nanoen.2019.05.008.
[5] M. Xiao, Z. Wang, K. Maeda, G. Liu, L. Wang, Addressing the stability challenge of photo(electro)catalysts towards solar water splitting, Chem. Sci. 14 (2023) 3415–3427, https://doi.org/10.1039/D2SC06981D.
[6] J.H. Kim, D. Hansora, P. Sharma, J.W. Jang, J.S. Lee, Toward practical solar hydrogen production – an artificial photosynthetic leaf-to-farm challenge, Chem. Soc. Rev. 48 (2019) 1908–1971, https://doi.org/10.1039/C8CS00699G.
[7] H. Tong, S. Ouyang, Y. Bi, N. Umezawa, M. Oshikiri, J. Ye, Nano-photocatalytic materials: possibilities and challenges, Adv. Mater. 24 (2012) 229–251, https://doi.org/10.1002/adma.201102752.
[8] R. Shi, Y. Cao, Y. Bao, Y. Zhao, G.I.N. Waterhouse, Z. Fang, L.Z. Wu, C.H. Tung, Y. Yin, T. Zhang, Self-assembled Au/CdSe nanocrystal clusters for plasmon-mediated photocatalytic hydrogen evolution, Adv. Mater. 29 (2017) 1700803, https://doi.org/10.1002/adma.201700803.
[9] F. Raziq, A. Hayat, M. Humayun, S.K.B. Mane, M.B. Faheem, A. Ali, Y. Zhao, S. Han, C. Cai, W. Li, D.C. Qi, J. Yi, X. Yu, M.B.H. Breese, F. Hassan, F. Ali, A. Mavlonov, K. Dhanabalan, X. Xiang, X. Zu, S. Li, L. Qiao, Photocatalytic solar fuel production and environmental remediation through experimental and DFT based research on CdSe-QDs-coupled P-doped-g-C3N4 composites, Appl. Catal. BEnviron. Energy 270 (2020) 118867, https://doi.org/10.1016/j.apcatb.2024.124264.
[10] Y.S. Chang, P.Y. Hsieh, T.F. Mark Chang, C.Y. Chen, M. Sone, Y.J. Hsu, Incorporating graphene quantum dots to enhance the photoactivity of CdSe-sensitized TiO2 nanorods for solar hydrogen production, J. Mater. Chem. A. 8 (2020) 13971–13979, https://doi.org/10.1039/D0TA02359K.
[11] K.A. Tsai, Y.J. Hsu, Graphene quantum dots mediated charge transfer of CdSe nanocrystals for enhancing photoelectrochemical hydrogen production, Appl. Catal. BEnviron. Energy 164 (2015) 271–278, https://doi.org/10.1016/j.apcatb.2014.09.034.
[12] S. Yuan, L. Feng, K. Wang, J. Pang, M. Bosch, C. Lollar, Y. Sun, J. Qin, X. Yang, P. Zhang, Q. Wang, L. Zou, Y. Zhang, L. Zhang, Y. Fang, J. Li, H.C. Zhou, Stable metal–organic frameworks: design, synthesis, and applications, Adv. Mater. 30 (2018) 1704303, https://doi.org/10.1002/adma.201704303.
[13] L. Jiao, Y. Wang, H.L. Jiang, Q. Xu, Metal–organic frameworks as platforms for catalytic applications, Adv. Mater. 30 (2018) 1703663, https://doi.org/10.1002/adma.201703663.
[14] G.L. Yang, X.J. Che, S.L. Hou, C.S. Cao, B. Zhao, Photocatalytic hydrogen evolution based on cobalt-organic framework with high water vapor adsorption, Inorg. Chem. 60 (2021) 1922–1929, https://doi.org/10.1021/acs.inorgchem.0c03397.
[15] S. Kampouri, F.M. Ebrahim, M. Fumanal, M. Nord, P.A. Schouwink, R. Elzein, R. Addou, G.S. Herman, B. Smit, C.P. Ireland, K.C. Stylianou, Enhanced visible-light-driven hydrogen production through MOF/MOF heterojunctions, ACS Appl. Mater. Interfaces 13 (2021) 14239–14247, https://doi.org/10.1021/acsami.0c23163.
[16] Z.D. Wang, Y. Zang, Z.J. Liu, P. Peng, R. Wang, S.Q. Zang, Opening catalytic sites in the copper-triazoles framework via defect chemistry for switching on the proton reduction, Appl. Catal. B Environ. Energy 288 (2021) 119941, https://doi.org/10.1016/j.apcatb.2021.119941.
[17] Y. He, C. Li, X.B. Chen, Z. Shi, S. Feng, Visible-light-responsive UiO-66(Zr) with DEfects Efficiently Promoting Photocatalytic CO2reduction, ACS Appl. Mater. Interfaces 14 (2022) 28977–28984, https://doi.org/10.1021/acsami.2c06993.
[18] T.F. Chen, L.Y. Wang, Y.F. Wang, H. Gao, J. He, G. Wang, X.F. Meng, Y.S. Wu, Y. H. Deng, C.Q. Wan, Facile strategy for efficient charge separation and high photoactivity of mixed-linker MOFs, ACS Appl. Mater. Interfaces 13 (2021) 20897–20905, https://doi.org/10.1021/acsami.1c04130.
[19] T. Wang, L. Zhang, J. Liu, X.X. Li, L. Yuan, S.L. Li, Y.Q. Lan, A viologen-functionalized metal-organic framework for efficient CO2 photoreduction reaction, ChemComm 58 (2022) 7507–7510, https://doi.org/10.1039/D2CC02650C.
[20] M.J. Kalmutzki, C.S. Diercks, O.M. Yaghi, Metal–organic frameworks for water harvesting from air, Adv. Mater. 30 (2018) 1704304, https://doi.org/10.1002/adma.201704304.
[21] M. Taheri, T. Tsuzuki, Photo-accelerated hydrolysis of metal organic framework ZIF-8, ACS Mater. Lett. 3 (2021) 255–260, https://doi.org/10.1021/acsmaterialslett.0c00522.
[22] L. Sun, M.G. Campbell, M. Dincă, Electrically conductive porous metal–organic frameworks, Angew. Chem. Int. Ed. 55 (2016) 3566–3579, https://doi.org/10.1002/anie.201506219.
[23] Y. Peng, S. Sanati, A. Morsali, H. García, Metal–organic frameworks as electrocatalysts, Angew. Chem. Int. Ed. 62 (2023) e202214707, https://doi.org/10.1002/anie.202214707.
[24] P. Thanasekaran, C.H. Su, Y.H. Liu, K.L. Lu, Weak interactions in conducting metal–organic frameworks, Coord. Chem. Rev. 442 (2021) 213987, https://doi.org/10.1016/j.ccr.2021.213987.
[25] H. Sepehrmansourie, H. Alamgholiloo, N.N. Pesyan, M.A. Zolfigol, A MOF-on-MOF strategy to construct double Z-scheme heterojunction for high-performance photocatalytic degradation, Appl. Catal. BEnviron. Energy 321 (2023) 122082, https://doi.org/10.1016/j.apcatb.2022.122082.
[26] L. Shen, M. Luo, Y. Liu, R. Liang, F. Jing, L. Wu, Noble-metal-free MoS2 co-catalyst decorated UiO-66/CdS hybrids for efficient photocatalytic H2 production, Appl. Catal. BEnviron. Energy 166–167 (2015) 445–453, https://doi.org/10.1016/j.apcatb.2014.11.056.
[27] A.A. Dubale, I.N. Ahmed, X.H. Chen, C. Ding, G.H. Hou, R.F. Guan, X. Meng, X. L. Yang, M.H. Xie, A highly stable metal–organic framework derived phosphorus doped carbon/Cu2O structure for efficient photocatalytic phenol degradation and hydrogen production, J. Mater. Chem. A. 7 (2019) 6062–6079, https://doi.org/10.1039/C8TA12544A.
[28] W. Xiao, M. Cheng, Y. Liu, J. Wang, G. Zhang, Z. Wei, L. Li, L. Du, G. Wang, H. Liu, Functional metal/carbon composites derived from metal–organic frameworks: insight into structures, properties, performances, and mechanisms, ACS Catal. 13 (2023) 1759–1790, https://doi.org/10.1021/acscatal.2c04807.
[29] W. Zhou, Y. Tang, X. Zhang, S. Zhang, H. Xue, H. Pang, MOF derived metal oxide composites and their applications in energy storage, Coord. Chem. Rev. 477 (2023) 214949, https://doi.org/10.1016/j.ccr.2022.214949.
[30] Z. Song, L. Zhang, K.D. Davis, X. Fu, J.L. Luo, X. Sun, Recent advances in MOF-derived single atom catalysts for electrochemical applications, Adv. Energy Mater. 10 (2020) 2001561, https://doi.org/10.1002/aenm.202001561.
[31] L. Fan, Y. Ji, G. Wang, J. Chen, K. Chen, X. Liu, Z. Wen, High entropy alloy electrocatalytic electrode toward alkaline glycerol valorization coupling with acidic hydrogen production, J. Am. Chem. Soc. 144 (2022) 7224–7235, https://doi.org/10.1021/jacs.1c13740.
[32] J.E. Zhou, J. Chen, Y. Peng, Y. Zheng, A. Zeb, X. Lin, Metal-organic framework-derived transition metal sulfides and their composites for alkali-ion batteries: a review, Coord. Chem. Rev. 472 (2022), https://doi.org/10.1016/j.ccr.2022.214781.
[33] T. Wang, H.K. Kim, Y. Liu, W. Li, J.T. Griffiths, Y. Wu, S. Laha, K.D. Fong, F. Podjaski, C. Yun, R.V. Kumar, B.V. Lotsch, A.K. Cheetham, S.K. Smoukov, Bottom-up formation of carbon-based structures with multilevel hierarchy from mof–guest polyhedra, J. Am. Chem. Soc. 140 (2018) 6130–6136, https://doi.org/10.1021/jacs.8b02411.
[34] J. Zhou, J. Zhao, R. Liu, Defect engineering of zeolite imidazole framework derived ZnS nanosheets towards enhanced visible light driven photocatalytic hydrogen production, Appl. Catal. BEnviron. Energy 278 (2020) 119265, https://doi.org/10.1016/j.apcatb.2020.119265.
[35] J. Qin, J. Wang, J. Yang, Y. Hu, M. Fu, D. Ye, Metal organic framework derivative-TiO2 composite as efficient and durable photocatalyst for the degradation of

toluene, Appl. Catal. BEnviron. Energy 267 (2020) 118667, https://doi.org/10.1016/j.apcatb.2020.118667.
[36] J. Lin, L. Wang, X. Meng, W. Li, N. Ren, L. Tao, J. Xiao, Q. Jing, Y. Song, H. Zhao, Improved light absorption enables highly efficient carbon dots luminescent solar concentrator, Appl. Phys. Lett. 126 (2025) 043904, https://doi.org/10.1063/5.0245924.
[37] W. Li, J. Lin, J. Li, Q. Jing, N. Ren, J. Xiao, H. Zhao, Y. Song, A. Vomiero, Wearable luminescent solar concentrators based on carbon dots crosslinked hydrogels, Nano Energy 148 (2026) 111674, https://doi.org/10.1016/j.nanoen.2025.111674.
[38] R.R. Ikreedeegh, M.A. Hossen, A. Sherryna, M. Tahir, Recent advances on synthesis and photocatalytic applications of MOF-derived carbon materials: a review, Coord. Chem. Rev. 510 (2024) 215834, https://doi.org/10.1016/j.ccr.2024.215834.
[39] Y. Su, S. Li, D. He, D. Yu, F. Liu, N. Shao, Z. Zhang, MOF-derived porous ZnO nanocages/rGO/carbon sponge-based photocatalytic microreactor for efficient degradation of water pollutants and hydrogen evolution, ACS Sustain. Chem. Eng. 6 (2018) 11989–11998, https://doi.org/10.1021/acssuschemeng.8b02287.
[40] C. Han, X. Zhang, S. Huang, Y. Hu, Z. Yang, T.T. Li, Q. Li, J. Qian, MOF-on-MOF-Derived Hollow Co3O4/In2O3 Nanostructure for Efficient Photocatalytic CO2 Reduction, Adv. Sci. 10 (2023) 2300797, https://doi.org/10.1002/advs.202300797.
[41] W.L. Ma, Y.Q. Zhang, W.Z. Li, J. Li, J. Luan, Fabrication of carbon-based materials derived from a cobalt-based organic framework for enhancing photocatalytic degradation of dyes, Dalton Trans. 53 (2024) 4314–4324, https://doi.org/10.1039/D3DT04055K.
[42] C.W. Tsao, M.J. Fang, Y.J. Hsu, Modulation of interfacial charge dynamics of semiconductor heterostructures for advanced photocatalytic applications, Coord. Chem. Rev. 438 (2021) 213876, https://doi.org/10.1016/j.ccr.2021.213876.
[43] J.P. Chang, C.Y. Wang, Y.J. Hsu, C.Y. Wang, Cu2O/UiO-66-NH2 composite photocatalysts for efficient hydrogen production from ammonia borane hydrolysis, Appl. Catal. A Gen. 650 (2023) 119005, https://doi.org/10.1016/j.apcata.2022.119005.
[44] Y.A. Chen, Y. Nakayasu, Y.C. Lin, J.C. Kao, K.C. Hsiao, Q.T. Le, K.D. Chang, M. C. Wu, J.P. Chou, C.W. Pao, T.F.M. Chang, M. Sone, C.Y. Chen, Y.C. Lo, Y.G. Lin, A. Yamakata, Y.J. Hsu, Double-Hollow Au@CdS Yolk@Shell Nanostructures as Superior Plasmonic Photocatalysts for Solar Hydrogen Production, Adv. Funct. Mater. 34 (2024) 2402392, https://doi.org/10.1002/adfm.202402392.
[45] J. Xiao, G. Ouyang, P. Liu, C.X. Wang, G.W. Yang, Reversible nanodiamond-carbon onion phase transformations, Nano Lett. 14 (2014) 3645–3652, https://doi.org/10.1021/nl5014234.
[46] M. Zeiger, N. Jäckel, V.N. Mochalin, V. Presser, Review: carbon onions for electrochemical energy storage, J. Mater. Chem. A. 4 (2016) 3172–3196, https://doi.org/10.1039/C5TA08295A.
[47] H. Zhang, W. Dai, R. Liu, J. Xiang, Y. Song, Y. Hou, H. Wei, P. Liu, B. Xu, J. Liang, J. Guo, ZIF-67-derived porous carbon nanosheets decorated with Co nanoflakes as bifunctional electrocatalysts for overall water splitting, ACS Appl. Nano Mater. 7 (2024) 12773–12782, https://doi.org/10.1021/acsanm.4c01317.
[48] M.A.N. Khan, P.K. Klu, C. Wang, W. Zhang, R. Luo, M. Zhang, J. Qi, X. Sun, L. Wang, J. Li, Metal-organic framework-derived hollow Co3O4/carbon as efficient catalyst for peroxymonosulfate activation, Chem. Eng. J. 363 (2019) 234–246, https://doi.org/10.1016/j.cej.2019.01.129.
[49] J. Zhao, X. Quan, S. Chen, Y. Liu, H. Yu, Cobalt nanoparticles encapsulated in porous carbons derived from core-shell ZIF67@ZIF8 as efficient electrocatalysts for oxygen evolution reaction, ACS Appl. Mater. Interfaces 9 (2017) 28685–28694, https://doi.org/10.1021/acsami.7b10138.
[50] H. Liu, Z. Guo, Q. Zhang, B. Jin, R. Peng, Zeolite imidazolate frameworks-67 precursor to fabricate a highly active Cobalt-embedded N-doped porous graphitized carbon catalyst for the thermal decomposition of ammonium perchlorate, ACS Omega 6 (2021) 25440–25446, https://doi.org/10.1021/acsomega.1c03427.
[51] L. Wei, Y. Wang, G. Jia, Y. Liang, Y. Liang, S. Qin, J. Qiu, X. Liu, H. Zhang, B. Gu, In-situ doped Zr, Ce and La promoter on ZIF-67 derived cobalt-based catalysts for syngas to liquid fuels with low CH4 selectivity and high stability, Fuel 393 (2025) 134929, https://doi.org/10.1016/j.fuel.2025.134929.
[52] J. Yan, Q. Wang, T. Wei, L. Jiang, M. Zhang, X. Jing, Z. Fan, Template-assisted low temperature synthesis of functionalized graphene for ultrahigh volumetric performance supercapacitors, ACS Nano 8 (2014) 4720–4729, https://doi.org/10.1021/nn500497k.
[53] S. Lettieri, A. Camisasca, M. Amora, A. Diaspro, T. Uchida, Y. Nakajima, K. Yanagisawa, T. Maekawa, S. Giordani, Far-red fluorescent carbon nano-onions as a biocompatible platform for cellular imaging, RSC Adv. 7 (2017) 45676–45681, https://doi.org/10.1039/C7RA09442F.
[54] A. Camisasca, A. Sacco, R. Brescia, S. Giordani, Boron/nitrogen-codoped carbon nano-onion electrocatalysts for the oxygen reduction reaction, ACS Appl. Nano Mater. 1 (2018) 5763–5773, https://doi.org/10.1021/acsanm.8b01430.
[55] E.M. Pérez, N. Martín, π-π Interactions in carbon nanostructures, Chem. Soc. Rev. 44 (2015) 6425–6433, https://doi.org/10.1039/C5CS00578G.
[56] C.P. Lee, W.F. Chen, T. Billo, Y.G. Lin, F.Y. Fu, S. Samireddi, C.H. Lee, J.S. Hwang, K.H. Chen, L.C. Chen, Beaded stream-like CoSe2 nanoneedle array for efficient hydrogen evolution electrocatalysis, J. Mater. Chem. A. 4 (2016) 4553–4561, https://doi.org/10.1039/C6TA00464D.
[57] J. Qi, Y.P. Lin, D. Chen, T. Zhou, W. Zhang, R. Cao, Autologous cobalt phosphates with modulated coordination sites for electrocatalytic water oxidation, Angew. Chem. Int. Ed. 59 (2020) 8917–8921, https://doi.org/10.1002/anie.202001737.
[58] Y. Zhu, J. Wang, T. Koketsu, M. Kroschel, J.M. Chen, S.Y. Hsu, G. Henkelman, Z. Hu, P. Strasser, J. Ma, Iridium single atoms incorporated in Co3O4 efficiently catalyze the oxygen evolution in acidic conditions, Nat. Commun. 13 (2022) 7754, https://doi.org/10.1038/s41467-022-35426-8.
[59] V.I. Klimov, D.W. Mcbranch, C.A. Leatherdale, M.G. Bawendi, Electron and hole relaxation pathways in semiconductor quantum dots, Phys. Rev. B 60 (1999) 13740, https://doi.org/10.1103/PhysRevB.60.13740.
[60] C. Burda, S. Link, M. Mohamed, M.E. Sayed, The relaxation pathways of CdSe nanoparticles monitored with femtosecond time-resolution from the visible to the IR: Assignment of the transient features by carrier quenching, J. Phys. Chem. B 105 (2001) 12286–12292, https://doi.org/10.1021/jp0124589.
[61] D.J. Norris, A. Sacra, C.B. Murray, M.G. Bawendi, Measurement of the Size Dependent Hole Spectrum in CdSe Quantum Dots, Phys. Rev. Lett. 72 (1994) 2612, https://doi.org/10.1103/PhysRevLett.72.2612.
[62] V.I. Klimov, Spectral and dynamical properties of multiexcitons in semiconductor nanocrystals, Annu. Rev. Phys. Chem. 58 (2007) 635–673, https://doi.org/10.1146/annurev.physchem.58.032806.104537.
[63] M. Wang, M. Wang, Y. Fu, S. Shen, Cobalt oxide and carbon modified hematite nanorod arrays for improved photoelectrochemical water splitting, Chin. Chem. Lett. 28 (2017) 2207–2211, https://doi.org/10.1016/j.cclet.2017.11.037.
[64] A.J. Abel, A.M. Patel, S.Y. Smolin, B. Opasanont, J.B. Baxter, Enhanced photoelectrochemical water splitting: Via SILAR-deposited Ti-doped hematite thin films with an FeOOH overlayer, J. Mater. Chem. A. 4 (2016) 6495–6504, https://doi.org/10.1039/C6TA01862A.
[65] D.M. Jang, Y. Myung, H.S. Im, Y.S. Seo, Y.J. Cho, C.W. Lee, J. Park, A.Y. Jee, M. Lee, Nanodiamonds as photocatalysts for reduction of water and graphene oxide, ChemComm 48 (2012) 696–698, https://doi.org/10.1039/C1CC16210A.
[66] E. Regulska, P. Olejnik, H. Zubyk, J.C. Horczak, M.N. Chaur, M. Tomczykowa, O. Butsyk, K. Brzezinski, L. Echegoyen, M.E.P. Brzezinska, Nanostructural catalyst: Metallophthalocyanine and carbon nano-onion with enhanced visible-light photocatalytic activity towards organic pollutants, RSC Adv. 10 (2020) 10910–10920, https://doi.org/10.1039/D0RA00896F.
[67] B. Liang, L. Zhang, W. Wang, G. Xu, W. Zhang, Y. Zhang, R. Zhang, L. Yang, L. Zhang, Nanodiamond core/onion-like carbon shell materials with excellent visible light photocatalytic activity, Mater. Res. Express 6 (2019) 045609, https://doi.org/10.1088/2053-1591/aafa23.
[68] C. Tang, E. Liu, J. Wan, X. Hu, J. Fan, Co3O4 nanoparticles decorated Ag3PO4 tetrapods as an efficient visible-light-driven heterojunction photocatalyst, Appl. Catal. BEnviron. Energy 181 (2016) 707–715, https://doi.org/10.1016/j.apcatb.2015.08.045.
[69] I.K. Moon, J. Lee, R.S. Ruoff, H. Lee, Reduced graphene oxide by chemical graphitization, Nat. Commun. 1 (2010) 73, https://doi.org/10.1038/ncomms1067.
[70] X. Zhou, X. Wang, X. Feng, K. Zhang, X. Peng, H. Wang, C. Liu, Y. Han, H. Wang, Q. Li, Loading Cd0.5Zn0.5S quantum dots onto onion-like carbon nanoparticles to boost photocatalytic hydrogen generation, ACS Appl. Mater. Interfaces 9 (2017) 22560–22567, https://doi.org/10.1021/acsami.7b05592.
[71] Z. Shi, L. Lan, Y. Li, Y. Yang, Q. Zhang, J. Wu, G. Zhang, X. Zhao, Co3O4/TiO2 nanocomposite formation leads to improvement in ultraviolet–visible-infrared-driven thermocatalytic activity due to photoactivation and photocatalysis–thermocatalysis synergetic effect, ACS Sustain. Chem. Eng. 6 (2018) 16503–16514, https://doi.org/10.1021/acssuschemeng.8b03602.
[72] L. Lan, Z. Shi, Q. Zhang, Y. Li, Y. Yang, S. Wu, X. Zhao, Defects lead to a massive enhancement in the UV-Vis-IR driven thermocatalytic activity of Co3O4 mesoporous nanorods, J. Mater. Chem. A. 6 (2018) 7194–7205, https://doi.org/10.1039/C8TA01362D.
[73] Y.H. Chiu, T.H. Lai, M.Y. Kuo, P.Y. Hsieh, Y.J. Hsu, Photoelectrochemical cells for solar hydrogen production: Challenges and opportunities, APL Mater. 7 (2019) 080901, https://doi.org/10.1063/1.5109785.
[74] P.Y. Hsieh, J.Y. Wu, T.F.M. Chang, C.Y. Chen, M. Sone, Y.J. Hsu, Near infrared-driven photoelectrochemical water splitting: review and future prospects, Arab. J. Chem. 13 (2020) 8372–8387, https://doi.org/10.1016/j.arabjc.2020.05.025.
[75] J.Y. Wu, Y.C. Wei, T. Torimoto, Y.A. Chien, C.Y. Chen, T.F.M. Chang, M. Sone, P. Y. Hsieh, Y.J. Hsu, Yolk@Shell nanostructures for water splitting: current development and future prospects, ACS Mater. Lett. (2024) 4066–4089, https://doi.org/10.1021/acsmaterialslett.4c00790.
[76] C.W. Tsao, S. Narra, J.C. Kao, Y.C. Lin, C.Y. Chen, Y.C. Chin, Z.J. Huang, W. H. Huang, C.C. Huang, C.W. Luo, J.P. Chou, S. Ogata, M. Sone, M.H. Huang, T.F. M. Chang, Y.C. Lo, Y.G. Lin, E.W.G. Diau, Y.J. Hsu, Dual-plasmonic Au@Cu7S4 yolk@shell nanocrystals for photocatalytic hydrogen production across visible to near infrared spectral region, Nat. Commun. 15 (2024) 413, https://doi.org/10.1038/s41467-023-44664-3.
[77] S. Wang, B. Zhu, M. Liu, L. Zhang, J. Yu, M. Zhou, Direct Z-scheme ZnO/CdS hierarchical photocatalyst for enhanced photocatalytic H2-production activity, Appl. Catal. BEnviron. Energy 243 (2019) 19–26, https://doi.org/10.1016/j.apcatb.2018.10.019.
[78] R. Shen, L. Zhang, N. Li, Z. Lou, T. Ma, P. Zhang, Y. Li, X. Li, W-N Bonds Precisely Boost Z-Scheme Interfacial Charge Transfer in g-C3N4/WO3 Heterojunctions for Enhanced Photocatalytic H2 Evolution, ACS Catal. 12 (2022) 9994–10003, https://doi.org/10.1021/acscatal.2c02416.
[79] Y.C. Lin, C.K. Peng, S.C. Lim, C.L. Chen, T.N. Nguyễn, T.T. Wang, M.C. Lin, Y. J. Hsu, S.Y. Chen, Y.G. Lin, Tailoring the surface oxygen engineering of a carbon-quantum-dot-sensitized ZnO@H-ZnO1-x multijunction toward efficient charge dynamics and photoactivity enhancement, Appl. Catal. BEnviron. Energy 285 (2021) 119846, https://doi.org/10.1016/j.apcatb.2020.119846.
[80] H.Q. Xu, S. Yang, X. Ma, J. Huang, H.L. Jiang, Unveiling Charge-Separation Dynamics in CdS/Metal–Organic Framework Composites for Enhanced

Photocatalysis, ACS Catal. 8 (2018) 11615–11621, https://doi.org/10.1021/acscatal.8b03233.
[81] C. Harris, P.V. Kamat, Photocatalysis with CdSe Nanoparticles in Confined Media: Mapping Charge Transfer Events in the Subpicosecond to Second Timescales, ACS Nano 3 (2009) 682–690, https://doi.org/10.1021/nn800848y.
[82] J.S. Nevins, K.M. Coughlin, D.F. Watson, Attachment of CdSe Nanoparticles to TiO2 via Aqueous Linker-Assisted Assembly: Influence of Molecular Linkers on Electronic Properties and Interfacial Electron Transfer, ACS Appl. Mater. Interfaces 3 (2011) 4242–4253, https://doi.org/10.1021/am200900c.
[83] F. Lapointe, M. Wolf, R.K. Campen, Y. Tong, Probing the Birth and Ultrafast Dynamics of Hydrated Electrons at the Gold/Liquid Water Interface via an Optoelectronic Approach, J. Am. Chem. Soc. 142 (2020) 18619–18627, https://doi.org/10.1021/jacs.0c08289.
[84] R. Yuan, Y. Guo, I. Gurgan, N. Siddique, Y.S. Li, S. Jang, G.A. Noh, S.H. Kim, Raman spectroscopy analysis of disordered and amorphous carbon materials: A review of empirical correlations, Carbon 238 (2025) 120214, https://doi.org/10.1016/j.carbon.2025.120214.
[85] C.C. Zhang, S. Hartlaub, I. Petrovic, B. Yilmaz, Raman Spectroscopy Characterization of Amorphous Coke Generated in Industrial Processes, ACS Omega 7 (2022) 2565–2570, https://doi.org/10.1021/acsomega.1c03456.
[86] V.I. Korepanov, H.O. Hamaguchi, E. Osawa, V. Ermolenkov, I.K. Lednev, B.J. M. Etzold, O. Levinson, B. Zousman, C.P. Epperla, H.C. Chang, Carbon structure in nanodiamonds elucidated from Raman spectroscopy, Carbon 121 (2017) 322–329, https://doi.org/10.1016/j.carbon.2017.06.012.
[87] S. Prawer, K.W. Nugent, D.N. Jamieson, J.O. Orwa, L.A. Bursill, J.L. Peng, The Raman spectrum of nanocrystalline diamond, Chem. Phys. Lett. 332 (2000) 93–97, https://doi.org/10.1016/S0009-2614(00)01236-7.
[88] V. Mochalin, S. Osswald, Y. Gogotsi, Contribution of functional groups to the raman spectrum of nanodiamond powders, Chem. Mat. 21 (2009) 273–279, https://doi.org/10.1021/cm802057q.
[89] Y. Zhang, Y. Hu, Z. Wang, T. Lin, X. Zhu, B. Luo, H. Hu, W. Xing, Z. Yan, L. Wang, Lithiation-Induced Vacancy Engineering of Co3O4 with Improved Faradic Reactivity for High-Performance Supercapacitor, Adv. Funct. Mater. 30 (2020) 2004172, https://doi.org/10.1002/adfm.202004172.
[90] L. Zhao, K. Liao, M. Pynenburg, L. Wong, N. Heinig, J.P. Thomas, K.T. Leung, Electro-oxidation of ascorbic acid by cobalt core-shell nanoparticles on a H-terminated Si(100) and by nanostructured cobalt-coated Si nanowire electrodes, ACS Appl. Mater. Interfaces 5 (2013) 2410–2416, https://doi.org/10.1021/am3021763.
[91] Y. Wang, J. Zhao, Z. Chen, F. Zhang, W. Guo, H. Lin, F. Qu, Construction of Z-scheme MoSe2/CdSe hollow nanostructure with enhanced full spectrum photocatalytic activity, Appl. Catal. B 244 (2019) 76–86, https://doi.org/10.1016/j.apcatb.2018.11.033.
[92] W. Han, Y. Chen, Y. Jiao, S. Liang, W. Li, G. Tian, ZIF-derived frame-in-cage hybrids of ZnSe-CdSe embedded within a N-doped carbon matrix for efficient photothermal conversion of CO2 into fuel, J. Mater. Chem. A Mater. 10 (2022) 17642–17651, https://doi.org/10.1039/d2ta03219h.